Upscaling of mass and thermal transports in porous media with heterogeneous combustion reactions

Chen Yang, Jean-François Thovert, Gérald Debenest

Upscaling of mass and thermal transports in porous media with heterogeneous combustion reactions

Chen Yang [a,*], Jean-François Thovert [b], Gérald Debenest [a]

[a] Université de Toulouse, INPT, UPS, IMFT (Institut de Mécanique des Fluides de Toulouse), 31400 Toulouse, France
[b] Institut Pprime, CNRS, SP2MI, BP 30179, 86962 Futuroscope Cedex, France

Keywords:
VAT
Heterogeneous chemical reaction
Local thermal non-equilibrium
Péclet number

A B S T R A C T

The present paper aims at an upscaled description of coupled heat and mass processes during solid–fluid combustion in porous media using volume-averaging theory (VAT). The fluid flows through the pores in a porous medium where a heterogeneous chemical reaction occurs at the fluid–solid interface. The chemical model is simplified into a single reaction step with Arrhenius kinetic law, but no assumption of local thermal equilibrium is made. An array of horizontal channels is chosen for the microstructure. The corresponding effective properties are obtained by solving analytically the closure problems over a representative unit cell. For a range of Péclet and Δ numbers, the results of the upscaled model are compared with microscale computations found in the literature. The results show that, under the same circumstances, the upscaled model is capable of predicting the combustion front velocity within an acceptable discrepancy, smaller than 1% when compared to the analytical solution. Furthermore, it has been found that for the Péclet and Δ numbers considered in this study, the fluid concentration and temperature profiles that stem from the present upscaled model are in accordance with those obtained using a microscale model.

1. Introduction

The propagation of combustion fronts in reactive porous media, which is usually referred to as smouldering or filtration combustion (FC), is a subject of interest for many applications. These include oil recovery using *in situ* combustion, coal gasification, fire safety, and foam combustion in a variety of situations. A broad review of all these domains is provided by Rein [1]. In all cases, an oxidation reaction is involved between an immobile fuel and an oxidizer, conveyed by a gas flow through the pore space.

Many contributions referring to this topic have been published in the past 40 years, such as the pioneer work of Aldushin et al. [2] where the structure of the filtration combustion wave was analyzed in one-dimensional geometries, followed by a series of papers using asymptotic methods for rapid, diffusive, co-current or counter-current filtration combustion waves [3–6]. All these contributions investigated the macroscale behaviors and the structure of solutions in effective porous media. More complex multicomponent, multiphysical, reactive problems were studied in this framework. For instance, Moallemi et al. [7] studied the smouldering in a two-dimensional scale solid material. They assumed a global single-step combustion reaction, and the associated transport problem was formulated via conservation equations for mass, species, linear momentum, and energy on the Darcy scale. Limits of flammability were compared to experimental tests. Rostami et al. [8] investigated the combustion of a porous biomass fuel, with a transient two-dimensional model without thermal equilibrium hypothesis and a complex multi-step chemistry. They showed the existence of a steady combustion regime depending on the ratio of oxygen to fuel contents. Rein et al. [9] studied the propagation of combustion fronts using a simplified transport model and complex chemistry of gas and solid components. Lapene et al. [10] developed a coupled simplified-transport model with chemistry to determine, by an optimization procedure, the effective multi-step reaction scheme of heavy-oil combustion in porous media. Fadaei et al. [11] investigated the combustion of reactive carbon in carbonate reservoirs by varying several parameters (flow rates, fraction of carbon and fraction of carbonates). No explicit link was made between local-scale phenomena and the heuristic macroscale model.

Local-scale solid–gas combustion was described in the review paper of Ohlemiller [12]. The structure and couplings were explained in detail, with a realistic description of a porous medium. The chemical coupling, the local-scale effects — i.e., local scale temperature effects — were addressed. According to Ohlemiller [12], all

* Corresponding author.
E-mail address: cyang@imft.fr (C. Yang).

http://dx.doi.org/10.1016/j.ijheatmasstransfer.2015.01.043

Nomenclature

a_V	interfacial surface area per unit cell volume (m^{-1})
A_0	pre-exponential factor ($m\ s^{-1}$)
A_{fm}	interfacial surface area between the fluid and solid phases (m^2)
b	closure variable
c_p	specific thermal capacity at constant pressure ($J\ kg^{-1}\ K^{-1}$)
$C_{f,in}$	concentration of oxidizer at the inlet (mol/m^3)
$C_{f,out}$	concentration of oxidizer at the outlet (mol/m^3)
ΔC_f	difference of oxidizer concentration between inlet and outlet (mol/m^3)
$C_{c,in}$	concentration of fuel at the inlet (mol/m^3)
$C_{c,int}$	concentration of fuel at the interface (mol/m^2)
$C_{c,out}$	concentration of fuel at the inlet (mol/m^3)
ΔC_c	difference of fuel concentration between inlet and outlet (mol/m^3)
C	concentration ($mol\ m^{-3}$)
D_f	mass diffusivity of fluid phase ($m^2\ s^{-1}$)
$\mathbf{D}_{eff}$	effective mass diffusivity tensor of fluid phase ($m^2\ s^{-1}$)
E	activation energy ($J\ mol^{-1}$)
F	arbitrary function of Taylor series
h	heat transfer coefficient ($J\ m^{-2}\ s^{-1}\ K^{-1}$)
H	heterogeneous reaction heat ($kJ\ mol^{-1}$)
H_c	heaviside step function accounting for the fuel exhaustion
$\langle H_c \rangle$	average step function
$H_{\langle c \rangle}$	binary function describing the presence or not of carbon at the macroscale
i, **j**	unit base vectors
I	unit matrix
k	thermal conductivity ($W\ K^{-1}\ m^{-1}$)
K	effective thermal conductivity tensor ($W\ K^{-1}\ m^{-1}$)
$\mathbf{K}_f$	effective permeability tensor (m^2)
l	microscopic characteristic length (m)
L	length of channel (m)
n_{fm}	normal unit vector from the fluid phase to the solid phase
p_f	pressure (Pa)
Pe_D	cell Péclet number based on the mass diffusivity
Pe_T	cell Péclet number based on the thermal diffusivity
$Pe_{F,s}$	thermal Péclet number based on solid thermal diffusivity and front speed velocity
q	heat generation ($kJ\ m^{-3}\ s^{-1}$)
r	special closure variable for the heterogeneous chemical reaction case
r_0	characteristic length associated with averaging volume
R	universal gas constant ($J\ mol^{-1}\ K^{-1}$)
s	closure variable
s_{rxn}	heterogeneous reaction rate ($mol\ m^{-2}\ s^{-1}$)
t	time (s)
T	temperature (K)
$T_{-\infty}$	reference upstream temperature (K)
$T_{+\infty}$	reference downstream temperature (K)
u	transport coefficient ($m\ s^{-1}$ or $W\ K^{-1}\ m^{-2}$)
U_F	combustion front velocity ($m\ s^{-1}$)
$\mathbf{v}_f$	velocity vector ($m\ s^{-1}$)
V	unit cell volume (m^3)
W	height of channel (m)
x, y	Cartesian coordinates (m)

Greek letters

ε	porosity
μ	dynamic viscosity ($kg\ m^{-1}\ s^{-1}$)
ρ	density ($kg\ m^{-3}$)
ψ	arbitrary variable
ς	arbitrary function of closure problem
ξ	heat distribution coefficient
φ	cell Thiele modulus
σ	Stephan–Boltzman constant ($W\ m^{-2}\ K^{-4}$)

Subscripts and superscripts

ad	adiabatic
c	concentration
f	fluid phase
F	combustion front
in	inlet
int	interface
out	outlet
m	solid phase
p	plateau

Special symbols

$\tilde{\phi}$	deviation from intrinsic average
$\langle \phi \rangle$	Darcian average
$\langle \phi \rangle^{f,m}$	intrinsic average

of the existing models in the literature were overly simplified and while they could be used for obtaining trends in front-velocity estimates and maximum-temperature approximations, for instance, they could not be predictive because of the lack of details in the description. Few references of studies on this scale can be found in the literature. Microscale or pore-scale studies are usually done to investigate the details of all the phenomena and to determine local effects, local thermal non-equilibrium, reaction shape, and speed, depending on the local properties. For example, based on a dual lattice, Lu and Yortos [13] developed a pore-network model to investigate the dynamics of forward filtration combustion in porous media. The pore-scale results showed that the overall macroscopic behavior of this process strongly depends on microscopic features, such as heterogeneity. Debenest et al. [14,15] performed 3D numerical calculations of smouldering processes in a detailed discretized image of porous medium, to demonstrate the ability of a numerical model proposed by Debenest et al. [16] to handle a variety of situations. Since combustion in porous media with heterogeneous chemical reactions is a complex phenomenon, which involves the transports of mass and heat as well as various chemical reactions, the numerical computations based on microscale structure are challenging. Upscaling approaches that treat a porous medium as an equivalent continuum have proved useful to overcome these limitations.

The published upscaling studies of reactive transport in porous media mainly focus on the mass or heat transfer. In an important reference paper, Oliveira and Kaviany [17] identified the length and time scales involved in heat and mass transports during combustion in porous media and determining the conditions for local equilibrium. Yet, they did not upscale the local-scale system of equations. Akkutlu and Yortsos [18] addressed theoretically *in situ* combustion and the explicit coupling between heat and mass transports with Arrhenius-type functions. Using a non-dimensional system, they obtained solutions for forward-filtration combustion and determined the effect of heat losses on the stability of the process. The link between the local-scale system of equations and the one pertaining to the macroscale has been addressed in detail in the pioneering works of Ryan [19] and Whitaker [20] on mass transfer

phenomena and coupled heterogeneous reactions. Related to our topic, Sahraoui and Kaviany [21] compared the volume-averaged treatment of adiabatic, premixed flame with direct numerical simulation in a porous medium. They showed that in spite of some shortcomings, the flame structure, thickness, speed, and excess temperature can be well predicted by volume-averaged treatments. Whitaker [22] upscaled the diffusion process in porous media with heterogeneous reactions. Moreover, Quintard and Whitaker [23] analyzed the coupled, nonlinear diffusion problem to derive the volume-averaged, multicomponent mass transport equations. Battiato et al. [24] upscaled the reaction–diffusion equations and compared the predictions of the macroscale equations to pore-scale results. More recently, Valdés-Parada and Aguilar-Madera [25] and Valdés-Parada et al. [26] carried out the upscaling process of mass transfer with both homogeneous and heterogeneous chemical reactions in porous media. The results showed that for the homogeneous case, the effective reaction rate is simply the product of its microscopic counterpart with the porosity, whereas the effective reaction rate can only be obtained by solving the corresponding closure problems for the heterogeneous case. All these studies were carried out in an isothermal case. Considering thermal transport in porous media with homogeneous and heterogeneous heat sources, Quintard and Whitaker [27,28] developed an upscaling analysis based on volume-averaging theory. The assumptions of local thermal equilibrium or non-equilibrium between the solid and fluid phases were discussed extensively. However, the heat source they treated was assumed to be constant and uniform, which is generally not realistic for combustion in porous media, where the coupling with chemical reactions involves highly non-linear Arrhenius-type kinetic laws.

In the present paper, we do not make such assumptions and derive a more general model by applying the volume-averaging theory of Quintard and Whitaker [27]. The heterogeneous chemical reaction, which is assumed to be of the first order Arrhenius-type, occurs at the interface between the solid and fluid phases. Moreover, local thermal equilibrium between the solid and fluid phases is not assumed *a priori*. The transport coefficients in the upscaled model are obtained by solving the corresponding closure problems in a stratified system. Eventually, the verification of the present upscaled model is conducted for a horizontal channel by comparison with direct numerical simulations on the pore-scale.

2. Upscaling of two-phase media with heterogeneous chemical reaction

In this study, we consider a rigid and immobile porous medium, saturated by a fluid phase as sketched in Fig. 1. We consider convection and diffusion in the mass transport equation, with reaction at the interface of the two phases, which is covered by the reactive material. The convection and conduction equations for heat transport are applied in the whole space with no contribution of convection within the solid phase. Radiative exchanges between the grains that face each other are not considered. The validity of this approximation depends on the typical pore size and on the expected range of temperature, and it can be assessed *a priori* for a particular application as discussed in Appendix A. We concentrate on studying the link between heat and mass transports and non-linear reactivity depending on Arrhenius-type kinetic functions. In all forthcoming developments, the subscript m refers to the solid phase, fully filled with inert solid, and subscript f refers to the fluid phase.

2.1. Microscale momentum, mass, and heat transfer equations

We assume that the fluid properties do not strongly depend on the temperature and concentrations; therefore, the momentum

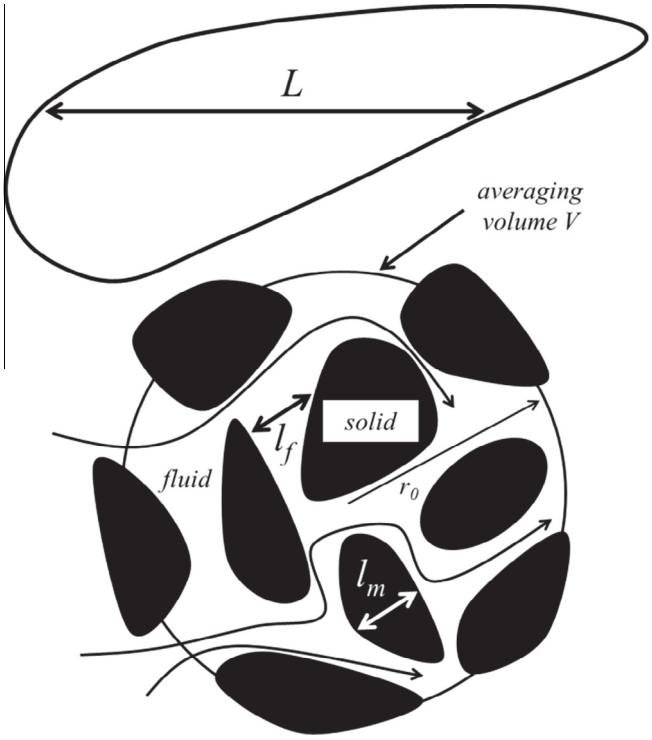

Fig. 1. Averaging volume for solid and fluid phases in the representative elementary volume (REV).

equation may be solved independently from the other transport equations. We also assume that the velocity is such low, i.e., the Reynolds number is small, so that Stokes equations may be used in the channels. Those assumptions are the same as those of Debenest et al. [16] and Yang and Debenest [32].

$$\nabla \cdot \mathbf{V}_f = 0 \quad \text{in} \quad V_f \tag{1}$$

$$-\nabla p_f + \mu_f \nabla^2 \mathbf{V}_f + \rho_f \mathbf{g} = 0 \quad \text{in} \quad V_f \tag{2}$$

$$\mathbf{V}_f = 0 \quad \text{at} \quad A_{fm} \tag{3}$$

Neglecting the variation of gas density strong approximation, which cannot be formally justified but whose consequences have been quantified and found acceptable in some cases. Yang and Debenest [32] performed numerical simulations of smouldering in a channel for both compressible and incompressible flows. The variations of density and dynamic viscosity of the gaseous mixture were taken into account in the compressible flow. The comparison between the two cases indicated that ignoring the variations of density and dynamic viscosity could result in significant discrepancies, but that for low values of Δ such as 0.1 and 0.5, the agreement between the incompressible and compressible results are acceptable. Since accounting for compressibility effects dramatically increases the computational time, the incompressible model is used in a first approximation.

The transport equation for the oxidizer conveyed by the fluid and the two energy transport equations in the solid and fluid phases read on the microscale:

$$\frac{\partial C_f}{\partial t} + \nabla \cdot (\mathbf{V}_f C_f) = \nabla \cdot (D_f \nabla C_f) \quad \text{in} \quad V_f \tag{4}$$

$$(\rho c_p)_m \frac{\partial T_m}{\partial t} = \nabla \cdot (k_m \nabla T_m) \quad \text{in} \quad V_m \tag{5}$$

$$(\rho c_p)_f \frac{\partial T_f}{\partial t} + (\rho c_p)_f \nabla \cdot (\mathbf{V}_f T_f) = \nabla \cdot (k_f \nabla T_f) \quad \text{in} \quad V_f \tag{6}$$

It is important to notice that we use the assumption of diluted species for the oxidizer transport equation. Multicomponent effects actually generate a diffusion matrix that is a function of the binary diffusion coefficients, the activity coefficients, and the mass fractions (see Quintard et al. [33]), but we simplify here the approach by specifying a constant value for the diffusion coefficient.

Combustion in porous media is complex and involves various chemical processes, as pointed out by Martins et al. [34]. For simplicity, we use the "one-film model" described by Turns [35], lumping all reactions in a single global one. The oxidizer in the gas phase reacts with the fuel located at the interface between the inert solid and fluid phases, and the reaction takes place as long as the fuel is not exhausted. The whole chemical scheme is summarized by a global exothermal heterogeneous reaction.

$$C + O_2 \rightarrow CO_2 + \Delta H_O \tag{7}$$

with $\Delta H_O = 395$ kJ/mol. The reaction products are regarded as passive and the description of their transport does not need to be included in the model. The kinetic law of reaction (7) is supposed to be of first order with respect to the oxidizer concentration C_f, with a rate coefficient given by Arrhenius law

$$s_{rxn} = A_0 H_c e^{-E/RT} C_f \tag{8}$$

A_0 is the pre-exponential factor, H_c is a Heaviside step function accounting for the fuel exhaustion, E is the activation energy, and R is the universal gas constant. The first order Arrhenius-type reaction rate is commonly used for the heterogeneous chemical reactions of carbon and oxygen (see for instance, Dutta et al. [36] and Žajdlík et al. [37]). The reaction rate depends on both the temperature and oxidizer concentration at the interface. Therefore, the oxidizer transport is fully coupled with the thermal problems.

The interfacial boundary conditions are

$$-\mathbf{n}_{fm} \cdot D_f \nabla C_f = s_{rxn} \quad \text{at} \quad A_{fm} \tag{9}$$

$$dC_{c,int}/dt = -s_{rxn} \quad \text{at} \quad A_{fm} \tag{10}$$

$$T_m = T_f \quad \text{at} \quad A_{fm} \tag{11}$$

$$\mathbf{n}_{fm} \cdot k_f \nabla T_f = \mathbf{n}_{fm} \cdot k_m \nabla T_m + s_{rxn} \times H \quad \text{at} \quad A_{fm} \tag{12}$$

where H is the heat of reaction, which is regarded as constant and independent of temperature. Theoretically, H depends on temperature, as do the heat capacity of the gas which is also regarded here as a constant. However, these approximations are milder than that regarding the gas incompressibility. Therefore, addressing the former without first curing the latter would result in an illusory gain in accuracy. All these issues should be addressed simultaneously, possibly in a future work.

2.2. Upscaling procedure

The upscaling process involves many steps that have been discussed at length in the literature. The details for the most well-known aspects can be found in Whitaker [22] and they are not repeated here. Under the assumption of scale separation, usually expressed as $l_f, l_m \ll r_o \ll L$, macroscale temperatures and concentration are defined by averages over the representative elementary volume (**REV**, Bear [38]) sketched in Fig. 1 as

$$\langle \psi_m \rangle = \frac{1}{V} \int_{V_m} \psi_m dV, \quad \langle \psi_m \rangle^m = \frac{1}{V_m} \int_{V_m} \psi_m dV \tag{13a}$$

$$\langle \psi_m \rangle = \varepsilon_m \langle \psi_m \rangle^m \tag{13b}$$

where

$$\varepsilon_m = V_m / V$$

All local variables are related to their intrinsic phase averages and corresponding deviations according to Gray's [39] spatial decomposition,

$$\mathbf{V}_f = \langle \mathbf{V}_f \rangle^f + \tilde{\mathbf{V}}_f, \qquad p_f = \langle p_f \rangle^f + \tilde{p}_f, \qquad C_f = \langle C_f \rangle^f + \tilde{C}_f,$$
$$T_m = \langle T_m \rangle^m + \tilde{T}_m, \qquad T_f = \langle T_f \rangle^f + \tilde{T}_f \tag{14}$$

Consider first the flow Eqs. (1)–(3). The upscaling of the single phase flow problem in a porous medium has been extensively studied in the past [40,41] and we simply state the result.

$$\nabla \cdot \langle \mathbf{V}_f \rangle = 0 \tag{15}$$

$$\langle \mathbf{V}_f \rangle = -\frac{\mathbf{K}_f}{\mu_f} \cdot (\nabla \langle p_f \rangle^f - \rho_f \mathbf{g}) \tag{16}$$

Eq. (16) is Darcy's law in which the permeability tensor $\mathbf{K}_f$ is given by a small-scale closure problem described explicitly in Whitaker [41], or in a different form more suitable for computations in Lasseux et al. [42]. Similarly, the macroscopic transport equations for solute (oxidizer) transport in the fluid and for energy transport in the solid and fluid phases result from volume-averaging theory (VAT) as

$$\varepsilon_f \frac{\partial \langle C_f \rangle^f}{\partial t} + \varepsilon_f \langle \mathbf{V}_f \rangle^f \cdot \nabla \langle C_f \rangle^f = \nabla \cdot \left[D_f \left(\varepsilon_f \nabla \langle C_f \rangle^f + \frac{1}{V} \int_{A_{fm}} \mathbf{n}_{fm} \tilde{C}_f dA \right) \right]$$
$$- \nabla \cdot \left\langle \tilde{\mathbf{V}}_f \tilde{C}_f \right\rangle + \frac{1}{V} \int_{A_{fm}} \mathbf{n}_{fm} \cdot D_f \nabla C_f dA \tag{17}$$

$$\varepsilon_m (\rho c_p)_m \frac{\partial \langle T_m \rangle^m}{\partial t} = \nabla \cdot \left[k_m \left(\varepsilon_m \nabla \langle T_m \rangle^m + \frac{1}{V} \int_{A_{mf}} \mathbf{n}_{mf} \tilde{T}_m dA \right) \right]$$
$$+ \frac{1}{V} \int_{A_{mf}} \mathbf{n}_{mf} \cdot k_m \nabla T_m dA \tag{18}$$

$$\varepsilon_f (\rho c_p)_f \frac{\partial \langle T_f \rangle^f}{\partial t} + \varepsilon_f (\rho c_p)_f \langle \mathbf{V}_f \rangle^f \cdot \nabla \langle T_f \rangle^f$$
$$= \nabla \cdot \left[k_f \left(\varepsilon_f \nabla \langle T_f \rangle^f + \frac{1}{V} \int_{A_{fm}} \mathbf{n}_{fm} \tilde{T}_f dA \right) \right] - (\rho c_p)_f \nabla \cdot \left\langle \tilde{\mathbf{V}}_f \tilde{T}_f \right\rangle$$
$$+ \frac{1}{V} \int_{A_{fm}} \mathbf{n}_{fm} \cdot k_f \nabla T_f dA \tag{19}$$

The reader could refer to Quintard and Whitaker [23,28] for more details behind the deviations of Eqs. (17)–(19). In order to close Eqs. (17)–(19), i.e., to eliminate any reference to the fluctuating variables, we need to (1) develop balance equations for the concentration and temperature deviations, $\tilde{C}_f$, $\tilde{T}_f$, and $\tilde{T}_m$, and (2) express these deviations as functions of macroscopic concentrations and temperatures. The first step is realized by applying decomposition Eq. (14) in the microscale Eqs. (4)–(6) and substracting the macroscale Eqs. (17)–(19). The resulting governing equations for the fluctuating quantities can be simplified owing to the following inequalities which result from the scale separation ($l_f, l_m \ll L$)

$$\nabla \cdot (D_f \nabla \tilde{C}_f) \gg \varepsilon_f^{-1} \nabla \cdot \left(\frac{D_f}{V} \int_{A_{fm}} \mathbf{n}_{fm} \tilde{C}_f dA \right), \quad \mathbf{V}_f \cdot \nabla \tilde{C}_f \gg \varepsilon_f^{-1} \nabla \cdot (\tilde{\mathbf{V}}_f \tilde{C}_f) \tag{20a,b}$$

$$\nabla \cdot (k_m \nabla \tilde{T}_m) \gg \varepsilon_m^{-1} \nabla \cdot \left(\frac{k_m}{V} \int_{A_{fm}} \mathbf{n}_{mf} \tilde{T}_m dA \right) \tag{21}$$

$$\nabla \cdot (k_f \nabla \tilde{T}_f) \gg \varepsilon_f^{-1} \nabla \cdot \left(\frac{k_f}{V} \int_{A_{fm}} \mathbf{n}_{fm} \tilde{T}_f dA \right), \quad (\rho c_p)_f \mathbf{v}_f \cdot \nabla \tilde{T}_f \gg \varepsilon_f^{-1} (\rho c_p)_f \nabla \cdot (\tilde{\mathbf{v}}_f \tilde{T}_f) \tag{22a,b}$$

Eventually, the simplified governing equations for the spatial fluctuations of oxidizer concentration, fluid and solid temperature read

$$\frac{\partial \tilde{C}_f}{\partial t}+\mathbf{V}_f\cdot\nabla\tilde{C}_f+\tilde{\mathbf{V}}_f\cdot\nabla\langle C_f\rangle^f=\nabla\cdot(D_f\nabla\tilde{C}_f)-\frac{\varepsilon_f^{-1}}{V}\int_{A_{fm}}\mathbf{n}_{fm}\cdot D_f\nabla\tilde{C}_f dA \quad \text{in} \quad V_f \tag{23}$$

$$(\rho c_p)_m\frac{\partial\tilde{T}_m}{\partial t}=\nabla\cdot(k_m\nabla\tilde{T}_m)-\frac{\varepsilon_m^{-1}}{V}\int_{A_{fm}}\mathbf{n}_{fm}\cdot k_m\nabla\tilde{T}_m dA \quad \text{in} \quad V_m \tag{24}$$

$$(\rho c_p)_f\frac{\partial\tilde{T}_f}{\partial t}+(\rho c_p)_f\mathbf{V}_f\cdot\nabla\tilde{T}_f+(\rho c_p)_f\tilde{\mathbf{V}}_f\cdot\nabla\langle T_f\rangle^f = \nabla\cdot(k_f\nabla\tilde{T}_f)-\frac{\varepsilon_f^{-1}}{V}\int_{A_{fm}}\mathbf{n}_{fm}\cdot k_f\nabla\tilde{T}_f dA \quad \text{in} \quad V_f \tag{25}$$

The associated interfacial boundary conditions are expressed as follows

$$-\mathbf{n}_{fm}\cdot D_f\nabla\tilde{C}_f=\mathbf{n}_{fm}\cdot D_f\nabla\langle C_f\rangle^f+s_{rxn} \quad \text{at} \quad A_{fm} \tag{26a}$$

$$\tilde{T}_m=\tilde{T}_f+\langle T_f\rangle^f-\langle T_m\rangle^m \quad \text{at} \quad A_{fm} \tag{26b}$$

$$\mathbf{n}_{fm}\cdot k_f\nabla\tilde{T}_f=\mathbf{n}_{fm}\cdot k_m\nabla\tilde{T}_m+\mathbf{n}_{fm}\cdot k_m\nabla\langle T_m\rangle^m - \mathbf{n}_{fm}\cdot k_f\nabla\langle T_f\rangle^f+s_{rxn}H \quad \text{at} \quad A_{fm} \tag{26c}$$

In practice, we assume the closure problem to be quasi-steady, i.e., the time derivatives in Eqs. (23)–(25) are discarded. Dynamic closures can be formulated by introducing time convolution products [43,44], but Davit et al. [44] showed that they can be approximated by the quasi-steady closures after some relaxation time.

2.3. Specific treatment for the reaction rate

So far, the reaction rate s_{rxn} which depends on the interfacial temperature and oxidizer concentration via Eq. (8) has not been explicited. This is done in the following, by expressing it as a function of the deviations $\tilde{T}_f$ or $\tilde{T}_m$ from the mean phase temperatures, and eliminating them by use of the matching condition Eq. (26b). An expression is eventually obtained, where only the concentration deviation $\tilde{C}_f$ is involved. This mathematical treatment can avoid the complex coupling of interface temperature and oxidizer concentration during the resolution of closure problems, and make it possible to obtain the analytical solutions of effective coefficients for some simple unit cells. This is the key for the account of a non-constant reaction rate in the upscaling procedure, which is the main contribution of the present work.

An arbitrary function F of the state variable can be expressed by using Taylor's theorem for multivariate functions truncated to first order as

$$F(T_{f,m},C_f)=F\left(\langle T_{f,m}\rangle^{f,m},\langle C_f\rangle^f\right) + \left[\left(T_{f,m}-\langle T_{f,m}\rangle^{f,m}\right)\frac{\partial F}{\partial T_{f,m}}\bigg|_{T_{f,m}=\langle T_{f,m}\rangle^{f,m},C_f=\langle C_f\rangle^f} +(C_f-\langle C_f\rangle^f)\frac{\partial F}{\partial C_f}\bigg|_{T_{f,m}=\langle T_{f,m}\rangle^{f,m},C_f=\langle C_f\rangle^f}\right]+\cdots \tag{27}$$

Using the decomposition laws Eq. (14), this reads

$$F(T_{f,m},C_f)=F\left(\langle T_{f,m}\rangle^{f,m},\langle C_f\rangle^f\right) + \left[\tilde{T}_{f,m}\frac{\partial F}{\partial T_{f,m}}\bigg|_{T_{f,m}=\langle T_{f,m}\rangle^{f,m},C_f=\langle C_f\rangle^f}+\tilde{C}_f\frac{\partial F}{\partial C_f}\bigg|_{T_{f,m}=\langle T_{f,m}\rangle^{f,m},C_f=\langle C_f\rangle^f}\right]+\cdots \tag{28}$$

Application of the expansion Eq. (28) to s_{rxn} as given by Eq. (8), in terms of the deviations $\tilde{C}_f$ and $\tilde{T}_m$ of the interfacial conditions from the mean oxidizer concentration and solid temperature yields

$$s_{rxn}=A_0H_ce^{-E/R\langle T_m\rangle^m}\langle C_f\rangle^f+\tilde{T}_mA_0H_c\frac{E}{R\left(\langle T_m\rangle^m\right)^2}e^{-E/R\langle T_m\rangle^m}\langle C_f\rangle^f + \tilde{C}_fA_0H_ce^{-E/R\langle T_m\rangle^m}+\boldsymbol{O}\left(\tilde{T}_m^2,\tilde{C}_f^2\right) \tag{29}$$

A similar expansion in terms of the deviation $\tilde{T}_f$ of the interfacial temperature from $\langle T_f\rangle^f$ leads to

$$s_{rxn}=A_0H_ce^{-E/R\langle T_f\rangle^f}\langle C_f\rangle^f+\tilde{T}_fA_0H_c\frac{E}{R\left(\langle T_f\rangle^f\right)^2}e^{-E/R\langle T_f\rangle^f}\langle C_f\rangle^f + \tilde{C}_fA_0H_ce^{-E/R\langle T_f\rangle^f}+\boldsymbol{O}\left(\tilde{T}_f^2,\tilde{C}_f^2\right) \tag{30}$$

Equating Eqs. (29) and (30) while taking the matching condition Eq. (26b) into account yields the following expression for the deviation $\tilde{T}_m$

$$\tilde{T}_m=\frac{\frac{E}{R\left(\langle T_f\rangle^f\right)^2}e^{-E/R\langle T_f\rangle^f}\left(\langle T_m\rangle^m-\langle T_f\rangle^f\right)-\left(e^{-E/R\langle T_m\rangle^m}-e^{-E/R\langle T_f\rangle^f}\right)}{\frac{E}{R\left(\langle T_m\rangle^m\right)^2}e^{-E/R\langle T_m\rangle^m}-\frac{E}{R\left(\langle T_f\rangle^f\right)^2}e^{-E/R\langle T_f\rangle^f}} + \frac{e^{-E/R\langle T_f\rangle^f}-e^{-E/R\langle T_m\rangle^m}}{\frac{E}{R\left(\langle T_m\rangle^m\right)^2}e^{-E/R\langle T_m\rangle^m}-\frac{E}{R\left(\langle T_f\rangle^f\right)^2}e^{-E/R\langle T_f\rangle^f}}\frac{\tilde{C}_f}{\langle C_f\rangle^f} \tag{31}$$

Finally, substituting Eq. (31) into Eq. (29), provides an expression for the chemical reaction rate which only depends on the concentration fluctuation $\tilde{C}_f$, in addition to the mean phase state variables,

$$s_{rxn}=H_cw_1\langle C_f\rangle^f+H_cw_2\tilde{C}_f \tag{32a}$$

where

$$w_1=c_1A_0e^{-E/R\langle T_m\rangle^m},\quad w_2=c_2A_0e^{-E/R\langle T_m\rangle^m} \tag{32b, c}$$

$$c_1=\left(1+\frac{\frac{E}{R\left(\langle T_f\rangle^f\right)^2}e^{-E/R\langle T_f\rangle^f}\left(\langle T_m\rangle^m-\langle T_f\rangle^f\right)-\left(e^{-E/R\langle T_m\rangle^m}-e^{-E/R\langle T_f\rangle^f}\right)}{e^{-E/R\langle T_m\rangle^m}-\left(\langle T_m\rangle^m/\langle T_f\rangle^f\right)^2e^{-E/R\langle T_f\rangle^f}}\right) \tag{32d}$$

and

$$c_2=\left(1+\frac{e^{-E/R\langle T_f\rangle^f}-e^{-E/R\langle T_m\rangle^m}}{e^{-E/R\langle T_m\rangle^m}-\left(\langle T_m\rangle^m/\langle T_f\rangle^f\right)^2e^{-E/R\langle T_f\rangle^f}}\right) \tag{32e}$$

In view of the mass flux boundary condition Eq. (26a), the surface integral in Eq. (23) can be expressed as

$$\frac{1}{V}\int_{A_{fm}}\mathbf{n}_{fm}\cdot D_f\nabla\tilde{C}_f dA=-\frac{1}{V}\int_{A_{fm}}s_{rxn}dA=-a_V\langle s_{rxn}\rangle_{fm} \tag{33a}$$

where

$$\langle s_{rxn}\rangle_{fm}=w_1\langle H_c\rangle\langle C_f\rangle^f+w_2\frac{1}{A_{fm}}\int_{A_{fm}}H_c\tilde{C}_f dA \tag{33b}$$

$\langle H_c\rangle$ is the average of H_c over the surface A_{fm}.

Even if H_c varies continuously in space, we will assume that the active surface of a REV is either fully active or completely depleted. It means that $\langle H_c\rangle$ is treated as a binary function denoted $H_{\langle c\rangle}$. It could take the following values:

$$\begin{aligned} H_{\langle c\rangle}&=0 \text{ when the surface is not active (carbon exhausted)}\\ H_{\langle c\rangle}&=1 \text{ when the surface is active (initial carbon content)}\end{aligned} \tag{33c}$$

Then we can rewrite Eq. (33b) using Eq. (33c) to obtain the average surface reaction rate

$$\langle s_{rxn}\rangle_{fm} = H_{\langle c\rangle}\left[w_1\langle C_f\rangle^f + w_2\frac{1}{A_{fm}}\int_{A_{fm}}\tilde{C}_f dA\right] \tag{33d}$$

Furthermore, the two surface integrals in Eqs. (24) and (25) can be related by exploiting the heat flux boundary condition Eq. (26c)

$$\frac{1}{V}\int_{A_{fm}}\mathbf{n}_{fm}\cdot k_f\nabla\tilde{T}_f dA = \frac{1}{V}\int_{A_{fm}}\mathbf{n}_{fm}\cdot k_m\nabla\tilde{T}_m dA + \frac{1}{V}\int_{A_{fm}} s_{rxn}\times H dA = \frac{1}{V}\int_{A_{fm}}\mathbf{n}_{fm}\cdot k_m\nabla\tilde{T}_m dA + a_V q_{fm} \tag{34}$$

where

$$q_{fm} = \langle s_{rxn}\rangle_{fm} H$$

At this stage, the non-linear contributions of the fluctuating parts of the state variables have been eliminated from the governing equations. The upscaled transport equations, in terms of the locally phase averaged variables read

$$\varepsilon_f\frac{\partial\langle C_f\rangle^f}{\partial t} + \varepsilon_f\langle\mathbf{V}_f\rangle^f\cdot\nabla\langle C_f\rangle^f = \nabla\cdot\left(\mathbf{D}_{eff}\cdot\nabla\langle C_f\rangle^f\right) + \nabla\cdot\left(\mathbf{u}_C\langle C_f\rangle^f\right) - a_V\langle s_{rxn}\rangle_{fm} \tag{35}$$

$$\varepsilon_m\frac{\partial\langle C_c\rangle^m}{\partial t} = -a_V\langle s_{rxn}\rangle_{fm} \tag{36}$$

$$\varepsilon_m(\rho c_p)_m\frac{\partial\langle T_m\rangle^m}{\partial t} = \nabla\cdot\left(\mathbf{K}_{mm}\cdot\nabla\langle T_m\rangle^m + \mathbf{K}_{mf}\cdot\nabla\langle T_f\rangle^f\right) + \mathbf{u}_{mm}\cdot\nabla\langle T_m\rangle^m + \mathbf{u}_{mf}\cdot\nabla\langle T_f\rangle^f - a_V h\left(\langle T_m\rangle^m - \langle T_f\rangle^f\right) + a_V\xi_m q_{fm} \tag{37}$$

$$\varepsilon_f(\rho c_p)_f\frac{\partial\langle T_f\rangle^f}{\partial t} + \varepsilon_f(\rho c_p)_f\langle\mathbf{V}_f\rangle^f\cdot\nabla\langle T_f\rangle^f = \nabla\cdot\left(\mathbf{K}_{ff}\cdot\nabla\langle T_f\rangle^f + \mathbf{K}_{fm}\cdot\nabla\langle T_m\rangle^m\right) + \mathbf{u}_{fm}\cdot\nabla\langle T_m\rangle^m + \mathbf{u}_{ff}\cdot\nabla\langle T_f\rangle^f + a_V h\left(\langle T_m\rangle^m - \langle T_f\rangle^f\right) + a_V\xi_f q_{fm} \tag{38}$$

They involve macroscale effective coefficients $\mathbf{K}_{\alpha\beta}$ and $\mathbf{u}_{\alpha\beta}$ (with α, $\beta = m$ or f), ξ_m, ξ_f, $\mathbf{D}_{eff}$, $\mathbf{u}_C$ and h, which can be determined by solving closure problems as described in Appendix B.It is important to note that the effective reaction rate in Eqs. (35)–(38) is the average reaction rate multiplied by the effective surface a_V. The effective coefficients ξ_m and ξ_f in Eqs. (37) and (38) are the volumetric repartition coefficients for the heat produced at the interface between the two phases.

3. Application to stratified porous media

This section is devoted to the application of the foregoing theoretical developments to a particular model of porous medium. We consider a medium made of periodic cells and calculate the effective parameters by solving the associated closure problems reported in Appendix B over this representative part of the medium. This assumption has been extensively discussed in several papers, but readers could refer to Chrysikopoulos et al. [45] or Eames and Bush [46]. It does not mean that the medium is seen as physically periodic but that the representative unit cell allows capturing the essential physical features of the involved processes.

A variety of unit-cell geometries have been used in the literature. Souto and Moyne [47] studied the dispersion tensor of two-dimensional periodic porous media is investigated numerically using the volume averaging method to calculate the dispersion tensor for ordered and disordered media. Yang and Nakayama [48] investigated analytically the effects of tortuosity and dispersion on the effective thermal conductivity of fluid-saturated porous media based on a 3D unit cell model, which embraces rectangular solids with connecting arms in an in-line arrangement. Kuwahara et al. [49] conducted exhaustive numerical experiments with in-line arrangement of square rods in order to determine the convective heat-transfer coefficient. Moreover, a numerical determination was performed by de Lemos and Saito [50] in cellular materials, in which the solid matrix is treated as an ordered array of elliptic rods. In the present study, however, the unit cell geometry shown in Fig. 2 is chosen to derive the effective properties. Furthermore, periodic boundary conditions are imposed on the unit-cell model, which can provide excellent agreement between theory and experiment for disordered systems, as claimed by Nozad et al. [51]. Recently, Yang and Debenest [32] studied on the microscale the combustion in a solid/gas system using the same geometry. It is important to note that microscale simulations are time-consuming, even for these simple geometries, as stated also by Debenest et al. [15].

In this geometry, analytical solutions for the transport coefficients in the energy equations Eqs. (37) and (38) can be readily found [52,28] and we simply report below the resulting macroscopic transport coefficients.

$$\mathbf{i}\cdot(\mathbf{K}_{mm})\cdot\mathbf{i}/k_f = \varepsilon_m k_m/k_f \tag{39a}$$

$$\mathbf{J}\cdot(\mathbf{K}_{mm})\cdot\mathbf{J}/k_f = \frac{k_m\varepsilon_m^2}{\varepsilon_f k_m + \varepsilon_m k_f} \tag{39b}$$

$$\mathbf{j}\cdot(\mathbf{K}_{mf})\cdot\mathbf{j}/k_f = \mathbf{j}\cdot(\mathbf{K}_{fm})\cdot\mathbf{j}/k_f = \frac{k_m\varepsilon_f\varepsilon_m}{\varepsilon_f k_m + \varepsilon_m k_f} \tag{39c}$$

$$\mathbf{i}\cdot(\mathbf{K}_{ff})\cdot\mathbf{i}/k_f = \varepsilon_f\left(1 + \frac{1}{2100}\frac{3\varepsilon_f k_m + 10\varepsilon_m k_f}{\varepsilon_f k_m + \varepsilon_m k_f}\varepsilon_f^2 Pe_T^2\right) \tag{39d}$$

$$\mathbf{j}\cdot(\mathbf{K}_{ff})\cdot\mathbf{j}/k_f = \frac{k_m\varepsilon_f^2}{\varepsilon_f k_m + \varepsilon_m k_f} \tag{39e}$$

$$\frac{(\mathbf{u}_{ff})\cdot\mathbf{i}}{(\rho c_p)_f\langle\mathbf{V}_f\rangle^f\cdot\mathbf{i}} = -\frac{2}{5}\frac{k_m\varepsilon_f^2}{\varepsilon_f k_m + \varepsilon_m k_f} \tag{39f}$$

$$\frac{(\mathbf{u}_{mf})\cdot\mathbf{i}}{(\rho c_p)_f\langle\mathbf{V}_f\rangle^f\cdot\mathbf{i}} = \frac{(\mathbf{u}_{fm})\cdot\mathbf{i}}{(\rho c_p)_f\langle\mathbf{V}_f\rangle^f\cdot\mathbf{i}} = \frac{1}{5}\frac{k_m\varepsilon_f^2}{\varepsilon_f k_m + \varepsilon_m k_f} \tag{39g}$$

$$\frac{a_V h(l_f + l_m)^2}{k_f} = \frac{12k_m}{\varepsilon_f k_m + \varepsilon_m k_f} \tag{39h}$$

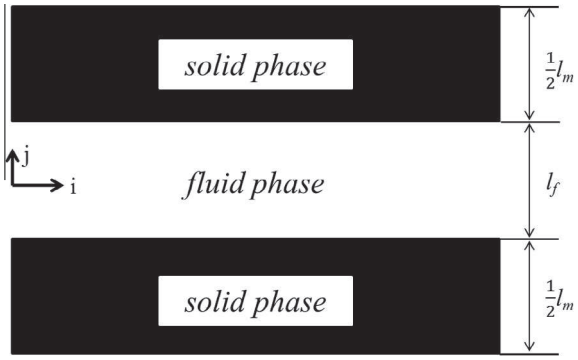

Fig. 2. Unit cell of a stratified system.

$$\xi_f = \frac{\varepsilon_m k_f}{\varepsilon_f k_m + \varepsilon_m k_f}, \quad \xi_m = 1 - \frac{\varepsilon_m k_f}{\varepsilon_f k_m + \varepsilon_m k_f} \tag{39i}$$

The last two terms describe the repartition of the heat between the two phases. They depend both on porosity and local scale conductivities. When dealing with solid/gas systems like rock/air, there is a strong contrast of conductivity between the two phases and so most of the heat produced by the reaction will be contained in the solid phase.

The original contribution of this study is the derivation of analytical solutions for the transport coefficients in the oxidizer transport equation in the stratified system, which read

$$\mathbf{i}\cdot(\mathbf{D}_{\mathit{eff}})\cdot\mathbf{i}/D_f = \varepsilon_f\left(1+\frac{1/2\left(\varepsilon_f c_2\varphi^2\right)^2+11\varepsilon_f c_2\varphi^2+20-35c_2\varphi^2/Pe_D}{350\left(\varepsilon_f c_2\varphi^2+2\right)\left(\varepsilon_f c_2\varphi^2+6\right)}\varepsilon_f^2 Pe_D^2\right) \tag{40a}$$

$$\mathbf{i}\cdot(\mathbf{D}_{\mathit{eff}})\cdot\mathbf{j}/D_f = \frac{\varepsilon_f^3 c_2\varphi^2}{10(\varepsilon_f c_2\varphi^2+2)(\varepsilon_f c_2\varphi^2+6)}Pe_D \tag{40b}$$

$$\mathbf{j}\cdot(\mathbf{D}_{\mathit{eff}})\cdot\mathbf{j}/D_f = \varepsilon_f \tag{40c}$$

$$(\mathbf{u}_C)\cdot\mathbf{i}(l_f+l_m)/D_f = -\frac{\varepsilon_f^2 c_1\varphi^2}{5(\varepsilon_f c_2\varphi^2+6)}Pe_D \tag{40d}$$

where the cell Thiele modulus φ is defined as

$$\varphi = \sqrt{\frac{A_0 e^{-E/R\langle T_m\rangle^m}(l_f+l_m)}{D_f}} \tag{41}$$

Note that the dispersion coefficient in Eq. (40a) is similar to the Taylor–Aris dispersion coefficient in the case of planar Poiseuille flow, which is a function of the square of the cell Péclet number Pe_D. However, the dispersion coefficient obtained here also depends on the cell Thiele modulus φ because of the heterogeneous chemical reaction. Valdés-Parada et al. [26] investigated the dependence of the effective diffusivity on the cell Thiele modulus for four types of microscopic structures. The results showed that the microstructures has only a moderate influence on the effective diffusivity for $\varphi < 1$. Whitaker [22] claimed that the convective transport term in Eq. (40d) generated by the heterogeneous reaction can be neglected in the case of diffusion in porous media. But, the contribution of this term to convective transport could be significant when convection itself is important, as pointed out by Paine et al. [53]. Moreover, the two surface-integral terms in Eq. (A5) which relates the mean reaction rate to the local average state variables are obtained as follows

$$(\mathbf{C_b})\cdot\mathbf{i}/(l_f+l_m) = \frac{\varepsilon_f\left(\varepsilon_f^2 c_2\varphi^2 Pe_D + 2\varepsilon_f Pe_D + 30\right)}{10(\varepsilon_f c_2\varphi^2+2)(\varepsilon_f c_2\varphi^2+6)} \tag{42a}$$

$$(\mathbf{C_b})\cdot\mathbf{j}/(l_f+l_m) = \frac{3\varepsilon_f}{(\varepsilon_f c_2\varphi^2+2)(\varepsilon_f c_2\varphi^2+6)} \tag{42b}$$

$$C_s = -\frac{\varepsilon_f c_1\varphi^2}{(\varepsilon_f c_2\varphi^2+6)} \tag{42c}$$

The transport coefficients which are not listed in the above are equal to zero. In these equations, the two cell Péclet numbers shown in Eqs. (39) and (40) are defined as:

$$Pe_D = \frac{\langle v_f\rangle^f(l_f+l_m)}{D_{O_2}} \tag{43a}$$

$$Pe_T = (\rho c_p)_f\frac{\langle v_f\rangle^f(l_f+l_m)}{k_f} \tag{43b}$$

4. Comparison of the macroscopic model with microscopic DNS calculations

4.1. Geometrical and physical setting

A comparison of the predictions of the present upscaled model with a direct numerical simulation (DNS) on the microscopic scale is conducted here, in order to validate the approach developed in this study. The physical geometry of the microscopic model is illustrated in Fig. 3. The system of equations to be solved is given by Eqs. (1)–(12). We base our analysis on the results of a previous study conducted by Yang and Debenest [32]. Moreover, the properties for oxygen and char combustion in the direct numerical simulation are presented in Table 1. Note that the activation energy is assumed to be constant. It has been pointed out by Tesner [54] that activation energy depends on temperature. However, Field et al. [55] showed that a constant activation energy for carbon oxidation is observed if temperature does not exceed 1650 K. Moreover, the channel width W is set to be 1×10^{-3} m, which is within the range of the experimental samples used by Fadaei [56].

A general analytical solution exists in a simplified 1D approach as illustrated in Debenest et al. [14]. A set of governing parameters, which has been defined in Debenest et al. [14,15] and Yang and Debenest [32], is briefly recalled here. Let us consider in a first step a one-dimensional situation in a very long domain. We suppose that the smouldering process has already run for an arbitrarily long time and that a steady regime has been reached. A reaction zone propagates with a velocity U_F, which defines the positive orientation of the x-axis. According to Fig. 3, we denote by ε_f and ε_m the volume fractions of the fluid and solid phases, with volumetric heat capacities $(\rho c_p)_f$ and $(\rho c_p)_m$. The gas flows in the open channel with a mean intersticial velocity $\langle v_f\rangle^f$. All the state variables are functions of the position, but, because of the stationary hypothesis, the temperature and the concentrations of the chemical species tend toward constant values on either side as x tends to $\pm\infty$. Hence, we introduce the two corresponding temperatures $T_{-\infty}$ and $T_{+\infty}$, the oxidizer concentrations $C_{f,in}$ at the inlet and $C_{f,in}-\Delta C_f = C_{f,out}$, and the initial fuel concentrations $C_{c,in}$ and $\Delta C_c = C_{c,in}-C_{c,out}$. The subscript *in* refers to inlet concentrations and the subscript *out* refers to outlet concentrations. The adiabatic temperature T_{ad} can be obtained from the ratio of the volumetric heat release to the volumetric heat capacity

$$T_{ad} = \frac{\varepsilon_m\Delta C_c H}{\left(\varepsilon_f(\rho c_p)_f + \varepsilon_m(\rho c_p)_m\right)} \tag{44}$$

The front velocity can be deduced from a global mass balance based on simple volumetric and stoichiometric arguments,

$$U_F = \frac{\varepsilon_f\Delta C_f}{\varepsilon_m\Delta C_c}\langle v_f\rangle^f \tag{45}$$

A global heat balance implies that

$$\underbrace{\left(\varepsilon_f(\rho c_p)_f + \varepsilon_m(\rho c_p)_m\right)}_{\text{accumulation}}\underbrace{(T_{-\infty}-T_{+\infty})}_{\text{convection}} + \varepsilon_f(\rho c_p)_f\langle v_f\rangle^f = \underbrace{\varepsilon_m\Delta C_c H U_F}_{\text{source term}} \tag{46}$$

The temperature increment across the reaction front can be obtained from Eq. (46) as

$$(T_{-\infty}-T_{+\infty}) = \frac{T_{ad}}{\Delta-1} \quad \text{with} \quad \Delta = \frac{\varepsilon_f(\rho c_p)_f\langle v_f\rangle^f}{\left(\varepsilon_f(\rho c_p)_f+\varepsilon_m(\rho c_p)_m\right)U_F} \tag{47}$$

We can then deduce that two regimes can exist, with a hot region upstream or downstream of the front region. They are called the reaction-leading and reaction-trailing cases by Schult et al. [5],

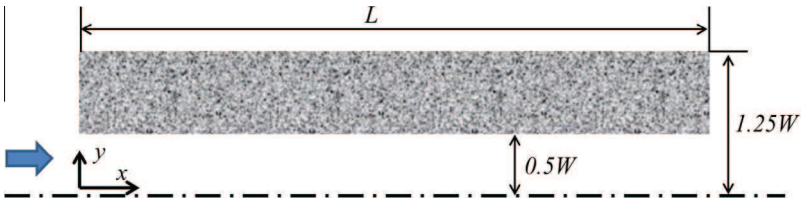

Fig. 3. Physical geometry for direct numerical simulation (DNS).

Table 1
Properties in the direct numerical simulations (DNS).

ρ_m	2100	kg/m^3	ρ_f	0.3	kg/m^3
$(c_p)_m$	800	J/kg K	$(c_p)_f$	1200	J/kg K
k_m	1	W/m K	k_f	0.025	W/m K
H	391.9	kJ/mol	D_f	2×10^{-4}	m^2/s
A_0	10	m/s	E	8314	J/mol
W	1×10^{-3}	m	L	0.3	m

respectively. For $\Delta > 1$, most of the heat produced in the reaction zone passes through the front and a plateau temperature T_p is then reached on the downstream side. The regime with $\Delta < 1$ leads to a plateau temperature upstream of the front zone. T_p can be deduced from Eq. (47) and is expressed as follows

$$T_p = \frac{T_{ad}}{|\Delta - 1|} \tag{48}$$

A detailed description of the analytical developments can be found in Debenest et al. [14], but the main results have been summarized here in order to provide a background to the readers. The last important parameter is the thermal Péclet number $Pe_{F,s}$ based on the combustion front velocity and defined as follows:

$$Pe_{F,s} = (\rho c_p)_m \frac{U_F W}{k_m} \tag{49}$$

As shown by Debenest et al. [14], increasing $Pe_{F,s}$ increases the local thermal disequilibrium between the solid and fluid phases in the reaction zone.

Since all the effective properties in the upscaled model are determined, the macroscale numerical simulations are performed over a 1D geometry with the same length, initial, and boundary conditions as those of the DNS geometry. The initial and boundary conditions are set as follows:

$$t = 0: \quad \langle T_f \rangle^f = \langle T_m \rangle^m = 500\ \text{K}, \quad \langle C_f \rangle^f = 0\ \text{mol/m}^3,$$
$$\langle C_c \rangle^m = 1954.4\ \text{mol/m}^3$$

$$\text{inlet}: \quad \langle T_f \rangle^f = 500\,K, \quad d\langle T_m \rangle^m / dx = 0,$$
$$\langle C_f \rangle^f = 4.188\,(\Delta = 0.1), 0.8376\,(\Delta = 0.5), \quad 0.2792\,(\Delta = 1.5)\ \text{mol/m}^3$$

$$\text{outlet}: \quad d\langle T_f \rangle^f / dx = 0, \quad d\langle T_m \rangle^m / dx, \quad d\langle C_f \rangle^f / dx = 0$$

It should be mentioned that, as shown in the inlet boundary conditions, the different values of Δ are obtained by varying the inlet oxidizer concentration while the fuel content remains constant. The adiabatic temperature T_{ad} can be easily deduced from Eq. (44) and is found equal to 455.8 K.

4.2. Results

The upscaled model is solved by using the COMSOL Multiphysics® package. The convergence criteria are set so that the residuals of all equations are less than 10^{-7}. Furthermore, a sensitivity analysis was conducted in order to guarantee that all of the results in the present study are independent of the grid step size.

First, the combustion front velocity predicted by the macroscale model is compared in Table 2 with those from the analytical formulation and from the DNS, for various values of Pe_D and Δ. It is seen that the present upscaled model is capable of predicting the location of the combustion front, which is defined as the abscissa value where the fuel content remaining in the solid phase is half of its initial value. The reaction zone can be broad, as shown by Debenest et al. [14], and this arbitrary definition of its position is chosen for the purpose of comparing the different approaches.

Since the prediction error of the combustion front velocity is close to zero, it can be ignored and the subsequent comparisons are performed at identical combustion front position rather than identical time.

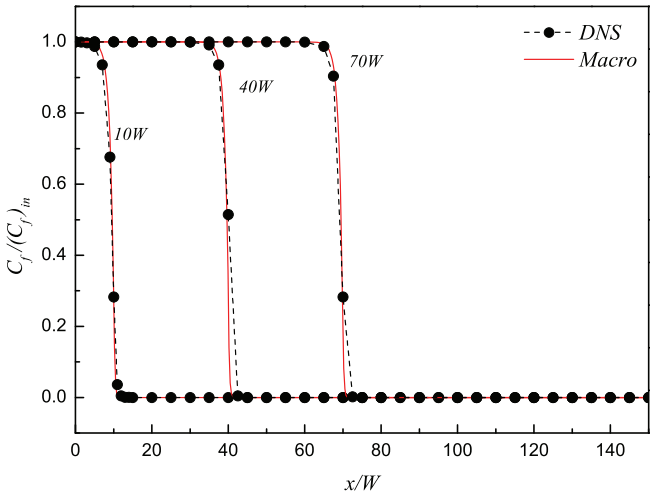

Fig. 4. Concentration profiles of the DNS and macroscale models in the direction of the combustion front propagation for $Pe_D = 2.5$ and $\Delta = 0.1$.

Table 2
Comparison of combustion front velocities.

	$Pe_{F,s}$	Analytical	DNS	Error DNS/analytical (%)	Macro	Error macro/analytical (%)
Combustion front velocity (m/s)						
$Pe_D = 2.5$, $\Delta = 0.1$	0.48	2.85×10^{-4}	2.88×10^{-4}	1.05	2.857×10^{-4}	0.24
$Pe_D = 25$, $\Delta = 0.1$	4.8	2.85×10^{-3}	2.79×10^{-3}	2.10	2.840×10^{-3}	0.35
$Pe_D = 25$, $\Delta = 0.5$	0.96	5.7×10^{-4}	5.66×10^{-4}	0.70	5.684×10^{-4}	0.28
$Pe_D = 25$, $\Delta = 1.5$	0.32	1.9×10^{-4}	1.9×10^{-4}	~ 0	1.896×10^{-4}	0.21

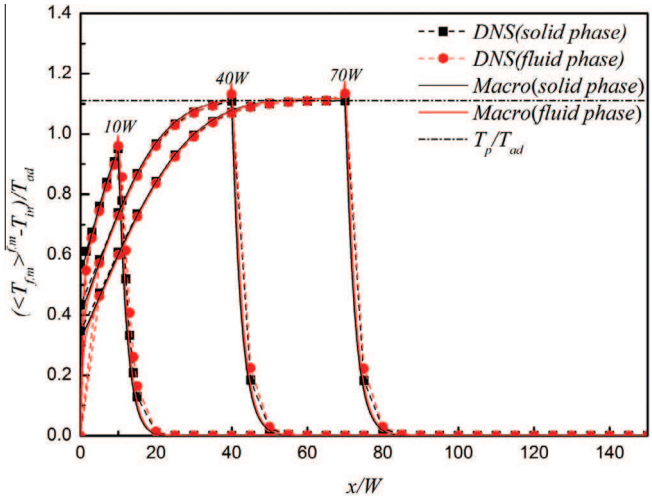

Fig. 5. Temperature profiles of the DNS and macroscale models in the direction of the combustion front propagation for $Pe_D = 2.5$ and $\Delta = 0.1$.

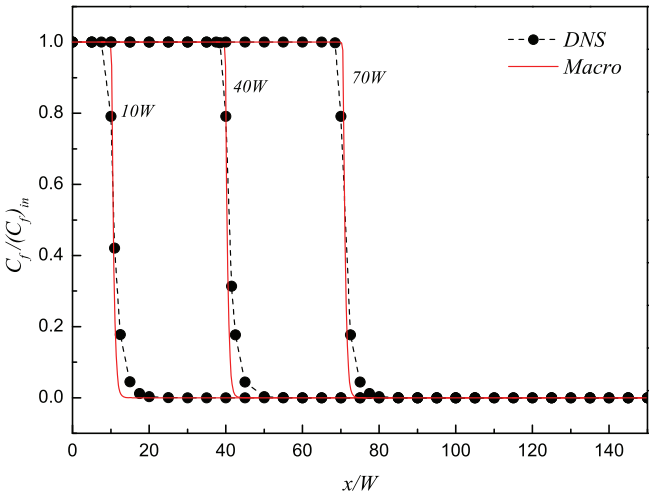

Fig. 6. Concentration profiles of the DNS and macroscale models in the direction of the combustion front propagation for $Pe_D = 25$ and $\Delta = 0.1$.

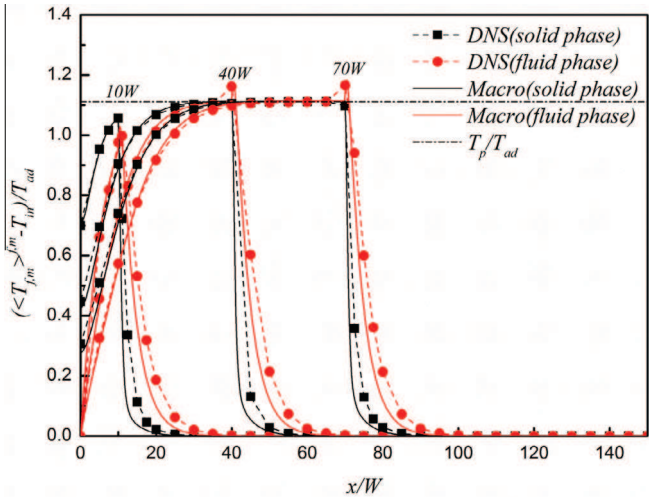

Fig. 7. Temperature profiles of the DNS and macroscale models in the direction of the combustion front propagation for $Pe_D = 25$ and $\Delta = 0.1$.

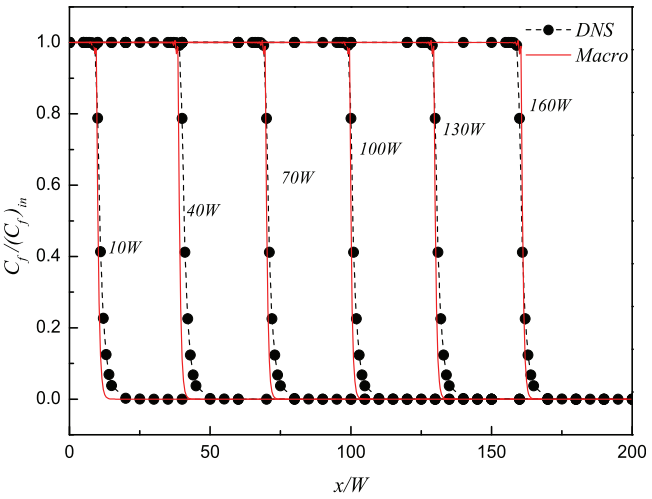

Fig. 8. Concentration profiles of the DNS and macroscale models in the direction of the combustion front propagation for $Pe_D = 25$ and $\Delta = 0.5$.

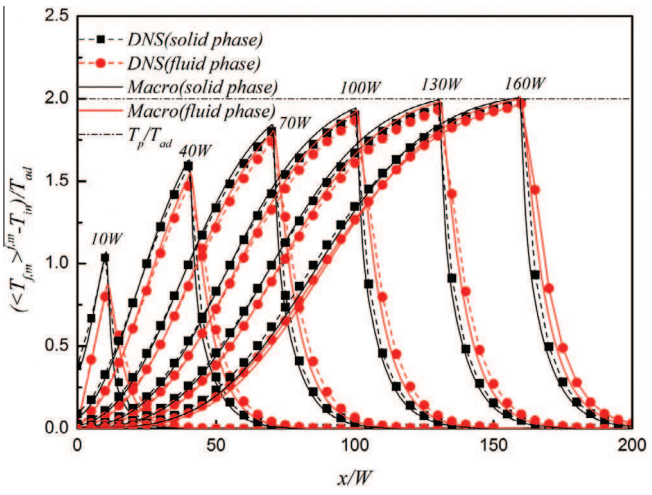

Fig. 9. Temperature profiles of the DNS and macroscale models in the direction of the combustion front propagation for $Pe_D = 25$ and $\Delta = 0.5$.

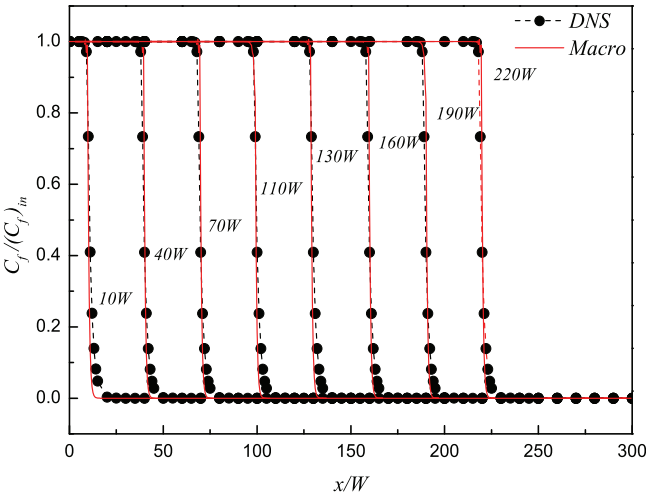

Fig. 10. Concentration profiles of the DNS and macroscale models in the direction of the combustion front propagation for $Pe_D = 25$ and $\Delta = 1.5$.

The oxidizer concentration and temperature profiles in both the fluid and solid phases based on the macroscale model and DNS are plotted in Figs. 4 and 5 in the case of $Pe_D = 2.5$ and $\Delta = 0.1$. The comparisons show that the predictions of DNS and upscaled model are in good agreements. Moreover, the temperature difference between the solid and fluid phases is so small that the local thermal equilibrium assumption is valid in this case. It is important to notice that the predicted plateau temperature T_p is obtained, which gives an important indication of the ability of the upscaling procedure to ensure a good representation of the complex and coupled phenomena.

In a first variant, Pe_D is increased while keeping Δ constant. Comparisons of the fluid concentration and temperature profiles from the macroscale model and DNS are illustrated in Figs. 6 and 7 for the case of $Pe_D = 25$ and $\Delta = 0.1$. The overall agreement is good, although slight discrepancies are visible. In the front region, the upscaled approach predicts the correct level of temperature, and the peak (above plateau temperature) is reproduced. The local thermal equilibrium assumption is invalid in this case in view of the significant temperature difference between the fluid and solid phases observed in Fig. 7. This emphasizes the necessity to use a two-temperature model such as the one developed here. The two-equation model provides a good approximation of the local scale problem because it captures more characteristic times. This is a necessary condition to reach accurate predictions of the reaction rate, which depends on both the temperature level and oxidizer concentration.

The increase of the Péclet number Pe_D with constant $\Delta = 0.1$ causes the rise of $Pe_{F,s}$ (see Table 2), and accordingly, differences between the solid and fluid phase temperatures are becoming noticeable, which indicates a thermal disequilibrium. The estimation of interfacial temperature deviation is required in the upscaling process, in order to correctly predict the effective reaction rate. For large values of $Pe_{F,s}$, the neglection of two high order terms in Eqs. (29), (30) during the estimation of the spatial deviation of the temperature of the solid phase at the interface would increase the prediction error of the effective reaction rate. This explains the larger discrepancy between the DNS and upscaled model observed in Fig. 7 than in Fig. 5. However, this discrepancy remains moderate

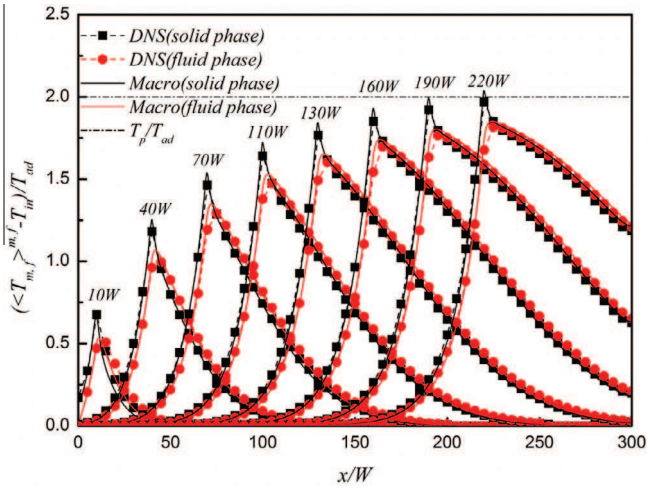

Fig. 11. Temperature profiles of the DNS and macroscale models in the direction of the combustion front propagation for $Pe_D = 25$ and $\Delta = 1.5$.

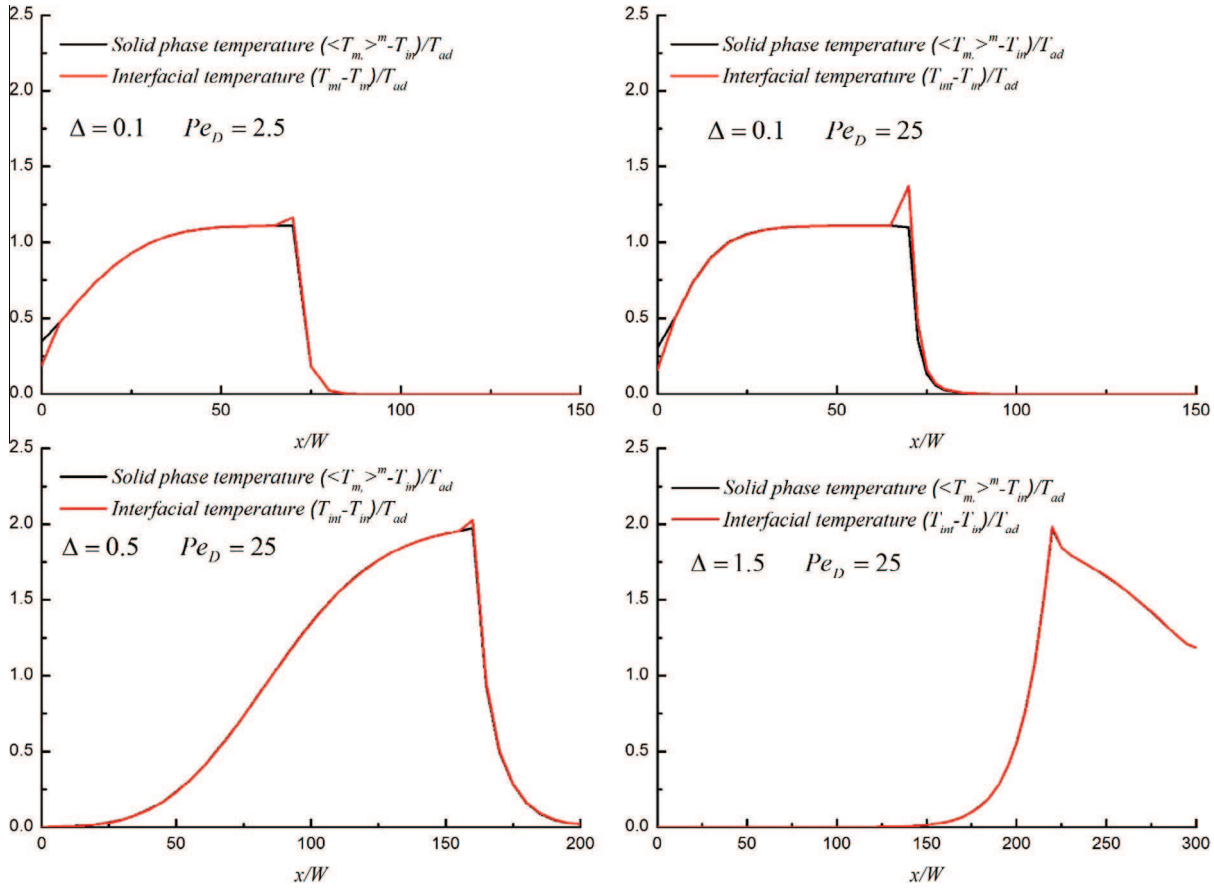

Fig. 12. Interfacial temperatures obtained using DNS compared to the average solid temperatures for the 4 cases.

and the macroscale model mimics the DNS results both in terms of temperature levels and form of the profiles.

In the next variants, the value of Δ is increased while keeping $Pe_D = 25$. The oxidizer concentration and temperature profiles from the macroscale model and from DNS are presented in Figs. 8 and 9 for the case of $Pe_D = 25$ and $\Delta = 0.5$. The oxidizer concentration from the macroscale model matches fairly well with that of DNS (Fig. 8). Moreover, the macroscale model reproduces with accuracy the temperatures obtained by DNS. The plateau temperature is barely reached when the reaction front has traveled $160W$. The upscaled model demonstrates here its ability to accurately describe transient regimes and capture the local scale dynamics.

All the foregoing simulations were conducted with $\Delta < 1$ and accordingly, most of the heat produced at the interface between the solid and fluid phases is left upstream of the reaction zone, as can be seen in Figs. 5, 7 and 9. This is called a reaction-leading structure. The last test addresses the case of $\Delta > 1$. The fluid concentration and temperature profiles from the macroscale model and DNS are plotted in Figs. 10 and 11 for $Pe_D = 25$ and $\Delta = 1.5$. Note that most of the heat released by the heterogeneous reaction is taken away downstream (Fig. 11), contrary to the previous observations for $\Delta < 1$. This is called a reaction-trailing structure (see Debenest et al. [14]). The plateau temperature appears downstream rather than upstream. A good agreement between the results of DNS and upscaling model is obtained. In the front region, both models predict a peak of the solid temperature, The forms of the temperature profiles are exactly the same, which indicates that the effective parameters, and mainly the effective conduction for all phases, are acceptable with respect to the upscaling procedure.

In summary, in view of the comparisons between the microscale model and macroscale approach performed for various Pe_D and Δ in this section, several important facts have been noted:

- The combustion front velocity is well predicted by the upscaled approach, when compared to both analytical solution and microscale simulations. In all cases, errors are limited to 0.4% in the whole range of parameters covered by the tests.
- In all cases, the temperatures profiles from the microscale and macroscale approaches match fairly well. The most significant errors occur when $Pe_{F,s}$ is much larger than unity (second case in Table 2), suggesting that the amplitude of the local scale disequilibrium has an effect on the estimations of effective quantities. At the local scale, the values of temperature on the fluid/solid interface are those used to calculate the reaction rate. In Fig. 12, we compared those local scale temperature with the mean interfacial solid temperature. We observe a good agreement in all cases, except for $Pe_{F,s}$ greater than one. Then, this suggests to use local non-equilibrium model.

Possible avenues to improve the accuracy of the upscaled model might consist in (1) reconsider the simplifications made during the upscaling procedure; (2) include higher-order terms in the expansion for the heterogeneous reaction rate in Eq. (29), which would introduce some other closure variables.

5. Conclusions

In this study, we have presented the coupled system of equations describing solid–gas combustion at the local scale in porous media, in order to explore the possibility of deriving a corresponding set of equations on the Darcy scale. The main challenge was to express the local scale boundary condition for the heat and mass transport problems. This was achieved by using a first order Taylor's expansion theorem for multivariate functions. Then, a macroscale model in a general non-equilibrium form was obtained in the framework of volume-averaging theory. A set of closure variables have been chosen, and the associated additional closure problems have been written.

For the purpose of determining the closure variables, a simple unit-cell model was chosen, namely the stratified system. In this simple geometry, all the effective properties could be calculated analytically, i.e., effective dispersion tensor, effective conduction tensor, and effective reaction rate.

Then, the predictions of the macroscale formulation have been compared to those of direct microscale simulations and to analytical results stemming from global balance arguments, in various conditions characterized by the Péclet number and the parameter Δ which determines the combustion regime. The front velocities are in perfect agreement. The concentration and temperature profiles have been confronted. Their overall features are correctly predicted and the expected values are nearly obtained in all cases, even when Δ is greater than one. Noticeable errors in the temperature profiles occur only in situations of strong local thermal disequilibrium, associated with large values of the thermal Péclet number.

An avenue for their correction is the improvement of the linearization procedure in the treatment of the heterogeneous reaction rate governed by Arrhenius law, by including higher-order terms. This would require in turn the solution of additional closure problems for the determination of new closure variables. Another possibility is the implementation of a mixed model, coupling macroscale equations – for instance, for describing transport in the fluid phase – with a microscale equation in the other phase. This mixed approach would be similar to the one of Golfier et al. [57]. The other advantage of this method could be a correct treatment of the Arrhenius function, in its original form at the local scale without any linearization.

Conflict of interest

None declared.

Appendix A. Radiative heat transfers

Recent studies such as Leroy et al. [29] or Yang et al. [30] focused on the description of radiative heat transfers in porous media coupled with conduction and convection. Under certain circumstances, they can be described by the classical Rosseland approximation, whereby the radiative transfers are incorporated in a macroscopic description in the form of an equivalent radiative conductivity coefficient (see e.g., Sano et al. [31]). During a combustion process, these transfers can be expected to be particularly intense in the hot region where the exothermic reactions take place and therefore to influence the smouldering process. They can for instance reduce the temperature in the hotest spots, contribute to spread the heat released by the reaction over a wider region, and thereby cause the reaction front to thicken.

These effects are not included in the present modelisation, in view of the ranges of temperature and pore sizes. Note first that because of heat storage in the solid phase, the temperatures involved in smoldering processes are smaller than in open flames. On the other hand, the heat transfer between solid surfaces separated by a distance d is of the order of $4\sigma\, T^3 \Delta T$, i.e., the equivalent conductivity k_{rad} is $O(4\sigma\, d\, T^3)$. If it is much smaller than the thermal conductivity of usual mineral materials ($k_m \sim 1$ W/m K) or gases ($k_f \sim 0.1$ W/m K) in this range of temperature, the contribution of radiative transfers is small and can be neglected in a first approach. In view of Eq. (48), the criterion for the validity of this approximation reads

$$k_{rad} \approx 4\,\sigma\, d \left[T_{in} + \frac{T_{ad}}{|\Delta - 1|}\right]^3 \ll \min(k_f, k_m) \approx 0.1 \text{ W/m K}$$

Note that the prediction Eq. (48) of the peak temperature results from global balance arguments and does not depend on the microstructure geometry. Therefore, this criterion is not restricted to stratified media. It involves a typical pore size d, the initial temperature T_{in}, and the parameters T_{ad} and Δ which depend on the solid and gas compositions and heat capacities. All these quantities can be estimated and the criterion can be checked *a priori*. Alternatively, it can be checked a posteriori in view of the actual maximal temperature obtained in the simulations. It can then be assessed on a per case basis whether the dimensionless results in the present work can be safely applied with dimensional values of the parameters. The influence of Δ is particularly crucial, since $\Delta \to 1$ corresponds to the superadiabatic conditions where temperature raises to very large values and radiative transfers are of primary importance.

For instance, with a typical pore size of $d \sim 0.1$ mm, $T_{in} = 500$ K, $T_{ad} = 456$ K and $\Delta = 0.1$ (Figs. 5 and 7), the temperature does not exceed 1000 K, $k_{rad} \sim 0.02$ W/m K and the criterion is reasonably satisfied. Conversely, T reaches 1400 K if $\Delta = 0.5$ or 1.5 (Figs. 9 and 11), $k_{rad} \sim 0.06$ W/m K and the approximation is very questionable. However, with the same materials ($T_{ad} = 456$ K and $\Delta = 0.5$ or 1.5) but a lower initial temperature $T_{in} = 300$ K and a tighter medium with $d \sim 0.05$ mm, k_{rad} is again $\sim$0.02 W/m K.

Note that the arbitrary choice of the aperture $W = 1$ mm adopted in the simulations has no influence on the dimensionless results (assuming that radiative transfers can indeed be neglected). It is only a convenience for an easier comparison with the results of Fadaei [56]. Fadaei did not either consider radiation in his simulations, but in spite of a lower temperature range which never exceeds 500 °C in his simulations, the large aperture $W = 1$ mm causes k_{rad} to reach $\sim$0.10 W/m K, which is of the order of the gas thermal conductivity and therefore probably plays a significant role.

Appendix B. Closure problems

This appendix is devoted to the resolution of closure problems, and then, the effective properties determination. According to Quintard and Whitaker [27], this form of the closure problem suggests the following representations for $\tilde{C}_f$, $\tilde{T}_m$ and $\tilde{T}_f$. We will use the assumption that the REV is either fully active or depleted. All the closure problems written here are expressed using $H_{\langle c\rangle} = 1$.

$$\tilde{C}_f = \mathbf{b}_C \cdot \nabla\langle C_f\rangle^f + s_C\langle C_f\rangle^f + \zeta_C \tag{A1}$$

$$\tilde{T}_m = \mathbf{b}_{mm} \cdot \nabla\langle T_m\rangle^m + \mathbf{b}_{mf} \cdot \nabla\langle T_f\rangle^f + s_m\left(\langle T_m\rangle^m - \langle T_f\rangle^f\right) + r_m q_{fm} + \zeta_m \tag{A2}$$

$$\tilde{T}_f = \mathbf{b}_{fm} \cdot \nabla\langle T_m\rangle^m + \mathbf{b}_{ff} \cdot \nabla\langle T_f\rangle^f - s_f\left(\langle T_f\rangle^f - \langle T_m\rangle^m\right) + r_f q_{fm} + \zeta_f \tag{A3}$$

where ζ_C, ζ_m and ζ_f are arbitrary functions, $\mathbf{b}_C$, $\mathbf{b}_{mm}$, $\mathbf{b}_{mf}$, $\mathbf{b}_{fm}$, $\mathbf{b}_{ff}$, s_C, s_m and s_f are known as the closure variables. Moreover, r_m and r_f are the specific closure variables for the heterogeneous chemical reaction case, which determine how the heterogeneous heat source is distributed between the solid and fluid phases.

In order to evaluate the surface integral in Eq. (33d), Eq. (A1) is substituted into Eq. (33d) to obtain

$$\langle s_{rxn}\rangle_{fm} = w_1 H_{\langle c\rangle}\langle C_f\rangle^f + H_{\langle c\rangle}\left(C_s\langle C_f\rangle^f + \mathbf{C}_b\nabla\langle C_f\rangle^f\right)w_2 \tag{A4}$$

where

$$C_s = \frac{1}{A_{fm}}\int_{Afm} s_C dA \quad \text{and} \quad \mathbf{C}_\mathbf{b} = \frac{1}{A_{fm}}\int_{Afm} \mathbf{b}_C dA \tag{A5}$$

Note that $\langle s_{rxn}\rangle_{fm}$ is the effective heterogeneous reaction rate, which embraces the effects of two surface integrals of closure variables. Valdés-Parada et al. [26] also studied the effect of surface integral of closure variable on the effective heterogeneous rate coefficient with the consideration of diffusion and found that the effective heterogeneous rate coefficient decreases with the rise of cell Thiele modulus, and has a weak and moderate dependency with the pore-scale structure and porosity, respectively.

Problem 1. Substitution of Eqs. (A1)–(A3) into Eqs. (23)–(25) leads to the governing differential equations of closure variables. The first closure problem is associated with $\nabla\langle C_f\rangle^f$ and takes the following form.

$$\mathbf{V}_f \cdot \nabla\mathbf{b}_C + \tilde{\mathbf{V}}_f = D_f\nabla^2\mathbf{b}_C + \varepsilon_f^{-1}a_V w_2\mathbf{C}_\mathbf{b} \quad \text{in} \quad V_f \tag{A6}$$

$$-\mathbf{n}_{fm} \cdot \nabla\mathbf{b}_C = \mathbf{n}_{fm} + \mathbf{b}_C w_2/D_f, \quad \text{at} \quad A_{fm} \tag{A7}$$

$$\text{Periodicity}: \ \mathbf{b}_C(r + \ell_i) = \mathbf{b}_C(r), \quad i = 1,2,3 \tag{A8}$$

$$\text{Average}: \ \langle\mathbf{b}_C\rangle^m = 0 \tag{A9}$$

Problem 2. The term $\langle C_f\rangle^f$ is also a source in the closure problem for $\tilde{C}_f$. The boundary value problem associated with the closure variable for $\langle C_f\rangle^f$ is given by

$$\mathbf{V}_f \cdot \nabla s_C = D_f\nabla^2 s_C + \varepsilon_f^{-1}a_V w_1 + \varepsilon_f^{-1}a_V w_2 C_s \quad \text{in} \quad V_f \tag{A10}$$

$$-\mathbf{n}_{fm} \cdot \nabla s_C = w_1/D_f + s_C w_2/D_f \quad \text{at} \quad A_{fm} \tag{A11}$$

$$\text{Periodicity}: \ s_C(r + \ell_i) = s_C(r), \quad i = 1,2,3 \tag{A12}$$

$$\text{Average}: \ \langle s_C\rangle^f = 0 \tag{A13}$$

Problem 3. In what follows, the first closure problem for the temperatures is associated with $\nabla\langle T_m\rangle^m$ and takes the form

$$k_m\nabla^2\mathbf{b}_{mm} = \varepsilon_m^{-1}\mathbf{C}_{mm} \quad \text{in} \quad V_m \tag{A14}$$

$$\mathbf{b}_{mm} = \mathbf{b}_{fm} \quad \text{at} \quad A_{fm} \tag{A15}$$

$$\mathbf{n}_{mf} \cdot k_m\nabla\mathbf{b}_{mm} = \mathbf{n}_{mf} \cdot k_f\nabla\mathbf{b}_{fm} - \mathbf{n}_{mf}k_m \quad \text{at} \quad A_{fm} \tag{A16}$$

$$(\rho c_p)_f\mathbf{V}_f \cdot \nabla\mathbf{b}_{fm} = k_f\nabla^2\mathbf{b}_{fm} + \varepsilon_f^{-1}\mathbf{C}_{mm} \quad \text{in} \quad V_f \tag{A17}$$

$$\text{Periodicity}: \ \mathbf{b}_{mm}(r + \ell_i) = \mathbf{b}_{mm}(r), \quad \mathbf{b}_{fm}(r + \ell_i) = \mathbf{b}_{fm}(r), \quad i = 1,2,3 \tag{A18}$$

$$\text{Average}: \ \langle\mathbf{b}_{mm}\rangle^m = 0, \langle\mathbf{b}_{fm}\rangle^f = 0 \tag{A19}$$

where $\mathbf{C}_{mm}$ is the unknown integral represented by

$$\mathbf{C}_{mm} = \frac{1}{V}\int_{A_{mf}} \mathbf{n}_{mf} \cdot k_m\nabla\mathbf{b}_{mm} dA \tag{A20}$$

A detailed description of the evaluation of this unknown integral is given by Quintard et al. [50].

Problem 4. The term $\nabla\langle T_f\rangle^f$ is also a source in the closure problem for $\tilde{T}_m$ and $\tilde{T}_f$. The boundary value problem associated with the closure variable for $\nabla\langle T_f\rangle^f$ is given by

$$k_m\nabla^2\mathbf{b}_{mf} = \varepsilon_m^{-1}\mathbf{C}_{mf} \quad \text{in} \quad V_m \tag{A21}$$

$$\mathbf{b}_{mf} = \mathbf{b}_{ff} \quad \text{at} \quad A_{fm} \tag{A22}$$

$$\mathbf{n}_{mf}\cdot k_m\nabla\mathbf{b}_{mf}=\mathbf{n}_{mf}\cdot k_f\nabla\mathbf{b}_{ff}+\mathbf{n}_{mf}k_f \quad \text{at} \quad A_{fm} \tag{A23}$$

$$(\rho c_p)_f\tilde{\mathbf{V}}_f+(\rho c_p)_f\mathbf{V}_f\cdot\nabla\mathbf{b}_{ff}=k_f\nabla^2\mathbf{b}_{ff}+\varepsilon_f^{-1}\mathbf{C}_{mf} \quad \text{in} \quad V_f \tag{A24}$$

$$\text{Periodicity}: \ \mathbf{b}_{mf}(r+\ell_i)=\mathbf{b}_{mf}(r), \quad \mathbf{b}_{ff}(r+\ell_i)=\mathbf{b}_{ff}(r), \quad i=1,2,3 \tag{A25}$$

$$\text{Average}: \ \langle\mathbf{b}_{mf}\rangle^m=0, \quad \langle\mathbf{b}_{ff}\rangle^f=0 \tag{A26}$$

where $\mathbf{C}_{mf}$ is the unknown integral represented by

$$\mathbf{C}_{mf}=\frac{1}{V}\int_{A_{mf}}\mathbf{n}_{mf}\cdot k_m\nabla\mathbf{b}_{mf}dA \tag{A27}$$

Problem 5. Moving on to the source represented by $\langle T_m\rangle^m-\langle T_f\rangle^f$ in Eq. (26b), we construct the following boundary problem for the closure scalars s_m and s_f.

$$0=k_m\nabla^2 s_m+\varepsilon_m^{-1}(a_V h) \quad \text{in} \quad V_m \tag{A28}$$

$$s_f=s_m+1 \quad \text{at} \quad A_{fm} \tag{A29}$$

$$\mathbf{n}_{mf}\cdot k_m\nabla s_m=\mathbf{n}_{mf}\cdot k_f\nabla s_f \quad \text{at} \quad A_{fm} \tag{A30}$$

$$(\rho c_p)_f\mathbf{V}_f\cdot\nabla s_f=k_f\nabla^2 s_f-\varepsilon_f^{-1}(a_v h) \quad \text{in} \quad V_f \tag{A31}$$

$$\text{Periodicity}: \ s_m(\mathrm{r}+\ell_i)=s_m(r), \quad s_f(\mathrm{r}+\ell_i)=s_f(r), \quad i=1,2,3 \tag{A32}$$

$$\text{Average}: \ \langle s_m\rangle^m=0, \quad \langle s_f\rangle^f=0 \tag{A33}$$

In this closure problem, the undetermined constant is represented by

$$a_V h=\frac{1}{V}\int_{A_{mf}}\mathbf{n}_{fm}\cdot k_m\nabla s_m dA \tag{A34}$$

Problem 6. Therefore, the focus in the following part is to determine how the heterogeneous heat source is distributed between the matrix and fracture. The corresponding closure problem takes the form

$$k_m\nabla^2 r_m=a_v\varepsilon_m^{-1}\xi_m \quad \text{in} \quad V_m \tag{A35}$$

$$r_f=r_m \quad \text{at} \quad A_{fm} \tag{A36}$$

$$\mathbf{n}_{fm}\cdot k_f\nabla r_f=\mathbf{n}_{fm}\cdot k_m\nabla r_m+1 \quad \text{at} \quad A_{fm} \tag{A37}$$

$$(\rho c_p)_f\mathbf{V}_f\cdot\nabla r_f=k_f\nabla^2 r_f-a_v\varepsilon_f^{-1}\xi_f \quad \text{in} \quad V_f \tag{A38}$$

$$\text{Periodicity}: \ r_m(\mathrm{r}+\ell_i)=r_m(\mathrm{r}), \quad r_f(\mathrm{r}+\ell_i)=r_f(\mathrm{r}), \quad i=1,2,3 \tag{A39}$$

$$\text{Average}: \ \langle r_m\rangle^m=0, \quad \langle r_f\rangle^f=0 \tag{A40}$$

where ξ_m and ξ_f are given by

$$\xi_m=\frac{1}{A_{mf}}\int_{A_{mf}}\mathbf{n}_{mf}\cdot k_m\nabla r_m dA, \quad \xi_f=\frac{1}{A_{fm}}\int_{A_{fm}}\mathbf{n}_{fm}\cdot k_f\nabla r_f dA \tag{A41}$$

According to the boundary condition Eq. (A37), we can get

$$\xi_f+\xi_m=1 \tag{A42}$$

After determining the terms associated with the spatial deviation temperatures, we can obtain the closed form of macroscopic governing equations given by

$$\varepsilon_f\frac{\partial\langle C_f\rangle^f}{\partial t}+\varepsilon_f\langle\mathbf{V}_f\rangle^f\cdot\nabla\langle C_f\rangle^f=\nabla\cdot\left(\mathbf{D}_{eff}\cdot\nabla\langle C_f\rangle^f\right)+\nabla\cdot\left(\mathbf{u}_C\langle C_f\rangle^f\right)-a_V\langle s_{rxn}\rangle_{fm} \tag{A43}$$

for the concentration transport equation in the fluid phase, and

$$\varepsilon_m(\rho c_p)_m\frac{\partial\langle T_m\rangle^m}{\partial t}=\nabla\cdot\left(\mathbf{K}_{mm}\cdot\nabla\langle T_m\rangle^m+\mathbf{K}_{mf}\cdot\nabla\langle T_f\rangle^f\right)+\mathbf{u}_{mm}\cdot\nabla\langle T_m\rangle^m+\mathbf{u}_{mf}\cdot\nabla\langle T_f\rangle^f-a_V h\left(\langle T_m\rangle^m-\langle T_f\rangle^f\right)+a_V\xi_m q_{fm} \tag{A44}$$

for the energy equation in the solid phase, and

$$\varepsilon_f(\rho c_p)_f\frac{\partial\langle T_f\rangle^f}{\partial t}+\varepsilon_f(\rho c_p)_f\langle\mathbf{V}_f\rangle^f\cdot\nabla\langle T_f\rangle^f=\nabla\cdot\left(\mathbf{K}_{ff}\cdot\nabla\langle T_f\rangle^f+\mathbf{K}_{fm}\cdot\nabla\langle T_m\rangle^m\right)+\mathbf{u}_{fm}\cdot\nabla\langle T_m\rangle^m+\mathbf{u}_{ff}\cdot\nabla\langle T_f\rangle^f+a_V h\left(\langle T_m\rangle^m-\langle T_f\rangle^f\right)+a_V\xi_f q_{fm} \tag{A45}$$

for the energy equation in the fluid phase. Note that the transport coefficients are defined by

$$\mathbf{D}_{eff}=\varepsilon_f D_f\mathbf{I}+\frac{D_f}{V}\int_{A_{mf}}\mathbf{n}_{fm}\mathbf{b}_C dA-\left\langle\tilde{\mathbf{V}}_f\mathbf{b}_C\right\rangle \tag{A46}$$

$$\mathbf{K}_{mm}=\varepsilon_m k_m\mathbf{I}+\frac{k_m}{V}\int_{A_{mf}}\mathbf{n}_{mf}\mathbf{b}_{mm}dA \tag{A47}$$

$$\mathbf{K}_{mf}=\frac{k_m}{V}\int_{A_{mf}}\mathbf{n}_{mf}\mathbf{b}_{mf}dA \tag{A48}$$

$$\mathbf{K}_{ff}=\varepsilon_f k_f\mathbf{I}+\frac{k_f}{V}\int_{A_{mf}}\mathbf{n}_{fm}\mathbf{b}_{ff}dA-(\rho c_p)_f\left\langle\tilde{\mathbf{V}}_f\mathbf{b}_{ff}\right\rangle \tag{A49}$$

$$\mathbf{K}_{fm}=\frac{k_f}{V}\int_{A_{mf}}\mathbf{n}_{fm}\mathbf{b}_{fm}dA-(\rho c_p)_f\left\langle\tilde{\mathbf{V}}_f\mathbf{b}_{fm}\right\rangle \tag{A50}$$

In addition, the heat transfer coefficient is given by

$$a_v h=\frac{1}{V}\int_{A_{mf}}\mathbf{n}_{fm}\cdot k_m\nabla s_m dA \tag{A50}$$

The five non-traditional convective transport terms in Eqs. (A43)–(A45) depend on the coefficients $\mathbf{u}_C$, $\mathbf{u}_{mm}$, $\mathbf{u}_{mf}$, $\mathbf{u}_{fm}$ and $\mathbf{u}_{ff}$ that are determined by

$$\mathbf{u}_C=\frac{D_f}{V}\int_{A_{mf}}\mathbf{n}_{fm}s_C dA-\left\langle\tilde{\mathbf{V}}_f s_C\right\rangle \tag{A51}$$

$$\mathbf{u}_{mm}=\frac{1}{V}\int_{A_{mf}}\mathbf{n}_{mf}\cdot k_m\nabla\mathbf{b}_{mm}dA+\frac{k_m}{V}\int_{A_{mf}}\mathbf{n}_{mf}s_m dA \tag{A52}$$

$$\mathbf{u}_{mf}=\frac{1}{V}\int_{A_{mf}}\mathbf{n}_{mf}\cdot k_m\nabla\mathbf{b}_{mf}dA-\frac{k_m}{V}\int_{A_{mf}}\mathbf{n}_{mf}s_m dA \tag{A53}$$

$$\mathbf{u}_{fm}=\frac{1}{V}\int_{A_{mf}}\mathbf{n}_{fm}\cdot k_f\nabla\mathbf{b}_{fm}dA+\frac{k_f}{V}\int_{A_{mf}}\mathbf{n}_{fm}s_f dA-(\rho c_p)_f\left\langle\tilde{\mathbf{V}}_f s_f\right\rangle \tag{A54}$$

$$\mathbf{u}_{ff}=\frac{1}{V}\int_{A_{mf}}\mathbf{n}_{fm}\cdot k_f\nabla\mathbf{b}_{ff}dA-\frac{k_f}{V}\int_{A_{mf}}\mathbf{n}_{fm}s_f dA+(\rho c_p)_f\left\langle\tilde{\mathbf{V}}_f s_f\right\rangle \tag{A55}$$

References

[1] G. Rein, Smouldering combustion phenomena in science and technology, Int. Rev. Chem. Eng. 1 (2009) 3–18.
[2] A.P. Aldushin, B.S. Seplyarskii, K.G. Shkadinskii, Theory of filtrational combustion, Combust. Explosion Shock Waves 16 (1) (1980) 33–40.
[3] A.P. Aldushin, S.G. Kasparyan, Stability of stationary filtrational combustion waves, Combust. Explosion Shock Waves 17 (6) (1981) 615–625.
[4] D.A. Schult, B.J. Matkowsky, V.A. Volpert, A.C. Fernandez-Pello, Propagation and extinction of forced opposed flow smolder waves, Combust. Flame 101 (4) (1995) 471–490.
[5] D.A. Schult, B.J. Matkowsky, V.A. Volpert, A.C. Fernandez-Pello, Forced forward smolder combustion, Combust. Flame 104 (1) (1996) 1–26.
[6] A. Bayliss, B.J. Matkowsky, D.A. Schult, Traveling waves in natural counterflow filtration combustion and their stability, SIAM J. Appl. Math. 58 (3) (1998) 806–852.
[7] M.K. Moallemi, H. Zhang, S. Kumar, Numerical modeling of two-dimensional smoldering processes, Combust. Flame 95 (1) (1993) 170–182.
[8] A. Rostami, J. Murthy, M. Hajaligol, Modeling of smoldering process in a porous biomass fuel rod, Fuel 83 (11) (2004) 1527–1536.
[9] G. Rein, A.C. Fernandez-Pello, D.L. Urban, Computational model of forward and opposed smoldering combustion in microgravity, Proc. Combust. Inst. 31 (2) (2007) 2677–2684.
[10] A. Lapene, G. Debenest, M. Quintard, L.M. Castanier, M.G. Gerritsen, A.R. Kovscek, Kinetics oxidation of heavy oil. 1. Compositional and full equation of state model, Energy Fuels 25 (11) (2011) 4886–4895.
[11] H. Fadaei, M. Sennoune, S. Salvador, A. Lapene, G. Debenest, Modelling of non-consolidated oil shale semi-coke forward combustion: influence of carbon and calcium carbonate contents, Fuel 95 (2012) 197–205.
[12] T.J. Ohlemiller, Modeling of smoldering combustion propagation, Prog. Energy Combust. Sci. 11 (4) (1985) 277–310.
[13] C. Lu, Y.C. Yortsos, Dynamics of forward filtration combustion at the pore-network level, AIChE J. 51 (4) (2005) 1279–1296.
[14] G. Debenest, V.V. Mourzenko, J.F. Thovert, Smouldering in fixed beds of oil shale grains: governing parameters and global regimes, Combust. Theor. Model. 9 (2) (2005) 301–321.
[15] G. Debenest, V.V. Mourzenko, J.F. Thovert, Three-dimensional microscale numerical simulation of smoldering process in heterogeneous porous media, Combust. Sci. Technol. 180 (12) (2008) 2170–2185.
[16] G. Debenest, V.V. Mourzenko, J.F. Thovert, Smouldering in fixed beds of oil shale grains. A three-dimensional microscale numerical model, Combust. Theory Model. 9 (1) (2005) 113–135.
[17] A.A.M. Oliveira, M. Kaviany, Nonequilibrium in the transport of heat and reactants in combustion in porous media, Prog. Energy Combust. Sci. 27 (5) (2001) 523–545.
[18] I.Y. Akkutlu, Y.C. Yortsos, The dynamics of in-situ combustion fronts in porous media, Combust. Flame 134 (3) (2003) 229–247.
[19] D. Ryan, Effective diffusivities in reactive porous media: a comparison between theory and experiments (Master's thesis), UC Davis, 1983.
[20] S. Whitaker, Mass transport and reaction in catalyst pellets, Transp. Porous Media 2 (3) (1987) 269–299.
[21] M. Sahraoui, M. Kaviany, Direct simulation vs volume-averaged treatment of adiabatic, premixed flame in a porous medium, Int. J. Heat Mass Transfer 37 (18) (1994) 2817–2834.
[22] S. Whitaker, The Method of Volume Averaging, Kluwer Academic Publishers, Dordrecht, 1999.
[23] M. Quintard, S. Whitaker, Coupled, nonlinear mass transfer and heterogeneous reaction in porous media, in: K. Vafai (Ed.), Handbook of Porous Media, CRC Press, Boca Raton, 2005, pp. 3–38.
[24] I. Battiato, D.M. Tartakovsky, A.M. Tartakovsky, T. Scheibe, On breakdown of macroscopic models of mixing-controlled heterogeneous reactions in porous media, Adv. Water Resour. 32 (11) (2009) 1664–1673.
[25] F.J. Valdés-Parada, J. Alvarez-Ramirez, On the effective diffusivity under chemical reaction in porous media, Chem. Eng. Sci. 65 (13) (2010) 4100–4104.
[26] F.J. Valdés-Parada, C.G. Aguilar-Madera, J. Alvarez-Ramirez, On diffusion, dispersion and reaction in porous media, Chem. Eng. Sci. 66 (10) (2011) 2177–2190.
[27] M. Quintard, S. Whitaker, One- and two-equation models for transient diffusion processes in two-phase systems, Adv. Heat Transfer 23 (C) (1993) 369–464.
[28] M. Quintard, S. Whitaker, Theoretical analysis of transport in porous media, in: H. Hadim, K. Vafai (Eds.), Handbook of Heat Transfer in Porous Media, Marcel Decker Inc, New York, 2000, pp. 1–52.
[29] V. Leroy, B. Goyeau, J. Taine, Coupled upscaling approaches for conduction, convection, and radiation in porous media: theoretical developments, Transp. Porous Media 98 (2) (2013) 323–347.
[30] C. Yang, Y. Sano, S. Iwase, A. Nakayama, Turbulent heat transfer analysis of silicon carbide ceramic foam as a solar volumetric receiver, Porous Media and its Applications in Science, Engineering, and Industry: Fourth International Conference, vol. 1453, AIP Publishing, 2012, pp. 115–120 (1).
[31] Y. Sano, A. Nakayama, S. Iwase, A local thermal nonequilibrium analysis of silicon carbide ceramic foam as a solar volumetric receiver, J. Sol. Energy Eng. 134 (2) (2012) 021006.
[32] C. Yang, G. Debenest, Numerical simulations for smouldering in a horizontal channel: comparisons between variable density-based formulation and incompressible one, Combust. Sci. Technol. 186 (2014) 1954–1974.
[33] M. Quintard, L. Bletzacker, D. Chenu, S. Whitaker, Nonlinear, multicomponent, mass transport in porous media, Chem. Eng. Sci. 61 (8) (2006) 2643–2669.
[34] M.F. Martins, S. Salvador, J.F. Thovert, G. Debenest, Co-current combustion of oil shale–Part 1: Characterization of the solid and gaseous products, Fuel 89 (1) (2010) 144–151.
[35] S.R. Turns, An Introduction to Combustion: Concepts and Applications, second ed., McGraw Hill, 1996.
[36] S. Dutta, C.Y. Wen, R. Belta, Reactivity of coal and char: 1. In carbon dioxide atmosphere, Ind. Eng. Chem. Process Des. 16 (1) (1977) 20–30.
[37] R. Žajdlík, Ľ. Jelemenský, B. Remiarová, J. Markoš, Experimental and modelling investigations of single coal particle combustion, Chem. Eng. Sci. 56 (2001) 1355–1361.
[38] J. Bear, Dynamics of Fluids in Porous Media, Elsevier, New York, 1972.
[39] W.G. Gray, A derivation of the equations for multi-phase transport, Chem. Eng. Sci. 30 (2) (1975) 229–233.
[40] E. Sanchez-Palencia, On the asymptotics of the fluid flow past an array of fixed obstacles, Int. J. Eng. Sci. 20 (12) (1982) 1291–1301.
[41] S. Whitaker, Flow in porous media: a theoretical derivation of Darcy's law, Transp. Porous Media 1 (1) (1986) 3–35.
[42] D. Lasseux, M. Quintard, S. Whitaker, Determination of permeability tensors for two-phase flow in homogeneous porous media: theory, Transp. Porous Media 24 (2) (1996) 107–137.
[43] C. Moyne, Two-equation model for a diffusive process in porous media using the volume averaging method with an unsteady-state closure, Adv. Water Resour. 20 (2) (1997) 63–76.
[44] Y. Davit, B.D. Wood, G. Debenest, M. Quintard, Correspondence between one- and two-equation models for solute transport in two-region heterogeneous porous media, Transp. Porous Media 95 (1) (2012) 213–238.
[45] C.V. Chrysikopoulos, P.K. Kitanidis, P.V. Roberts, Generalized Taylor–Aris moment analysis of the transport of sorbing solutes through porous media with spatially-periodic retardation factor, Transp. Porous Media 7 (2) (1992) 163–185.
[46] I. Eames, J.W.M. Bush, Longitudinal dispersion by bodies fixed in a potential flow, Proc. R. Soc. A Math. Phys. Eng. Sci. 455 (1990) (1999) 3665–3686.
[47] H.P.A. Souto, C. Moyne, Dispersion in two-dimensional periodic porous media, Part II: Dispersion tensor, Phys. Fluids 9 (8) (1997) 2253–2263.
[48] C. Yang, A. Nakayama, A synthesis of tortuosity and dispersion in effective thermal conductivity of porous media, Int. J. Heat Mass Transfer 53 (15) (2010) 3222–3230.
[49] F. Kuwahara, M. Shirota, A. Nakayama, A numerical study of interfacial convective heat transfer coefficient in two-energy equation model for convection in porous media, Int. J. Heat Mass Transfer 44 (6) (2001) 1153–1159.
[50] M.J.S. de Lemos, M.B. Saito, Heat transfer coefficient for cellular materials modelled as an array of elliptic rods, Adv. Eng. Mater. 11 (10) (2009) 837–842.
[51] I. Nozad, R.G. Carbonell, S. Whitaker, Heat conduction in multiphase systems—I: Theory and experiment for two-phase systems, Chem. Eng. Sci. 40 (5) (1985) 843–855.
[52] M. Quintard, M. Kaviany, S. Whitaker, Two-medium treatment of heat transfer in porous media: numerical results for effective properties, Adv. Water Resour. 20 (2) (1997) 77–94.
[53] M.A. Paine, R.G. Carbonell, S. Whitaker, Dispersion in pulsed systems—I: Heterogenous reaction and reversible adsorption in capillary tubes, Chem. Eng. Sci. 38 (11) (1983) 1781–1793.
[54] P.A. Tesner, The activation energy of gas reactions with solid carbon, in: Symposium (International) on Combustion, vol. 8, (1), 1961, pp. 807–814.
[55] M.A. Field, D.W. Gill, B.B. Morgan, P.G.W. Hawskey, Combustion of Pulverized Coal, The British Coal Utilization Research Assoc., Leatherhead, England, 1967. pp. 413.
[56] H. Fadaei, Etude de la récupération de bruts lourds en réservoir carbonaté fracturé par le procédé de combustion in situ (PhD Thesis), INP Toulouse, 2009.
[57] F. Golfier, M. Quintard, F. Cherblanc, B.A. Zinn, B.D. Wood, Comparison of theory and experiment for solute transport in highly heterogeneous porous medium, Adv. Water Resour. 30 (11) (2007) 2235–2261.